

A review on functionally graded materials and structures via additive manufacturing

LI, Yan ; FENG, Zuying; HAO, Liang; HUANG, Lijing; Xin, Chenxing; Wang, Yushen; BILOTTI, Emiliano; Essa, Khamis; ZHANG, Han; Li, Zheng ; Yan, Feifei; PEIJS, Ton

DOI:

[10.1002/admt.201900981](https://doi.org/10.1002/admt.201900981)

License:

Creative Commons: Attribution (CC BY)

Document Version

Publisher's PDF, also known as Version of record

Citation for published version (Harvard):

LI, Y, FENG, Z, HAO, L, HUANG, L, Xin, C, Wang, Y, BILOTTI, E, Essa, K, ZHANG, H, Li, Z, Yan, F & PEIJS, T 2020, 'A review on functionally graded materials and structures via additive manufacturing: from multi-scale design to versatile functional properties', *Advanced Materials Technologies*, vol. 5, no. 6, 1900981. <https://doi.org/10.1002/admt.201900981>

[Link to publication on Research at Birmingham portal](#)

General rights

Unless a licence is specified above, all rights (including copyright and moral rights) in this document are retained by the authors and/or the copyright holders. The express permission of the copyright holder must be obtained for any use of this material other than for purposes permitted by law.

- Users may freely distribute the URL that is used to identify this publication.
- Users may download and/or print one copy of the publication from the University of Birmingham research portal for the purpose of private study or non-commercial research.
- User may use extracts from the document in line with the concept of 'fair dealing' under the Copyright, Designs and Patents Act 1988 (?)
- Users may not further distribute the material nor use it for the purposes of commercial gain.

Where a licence is displayed above, please note the terms and conditions of the licence govern your use of this document.

When citing, please reference the published version.

Take down policy

While the University of Birmingham exercises care and attention in making items available there are rare occasions when an item has been uploaded in error or has been deemed to be commercially or otherwise sensitive.

If you believe that this is the case for this document, please contact UBIRA@lists.bham.ac.uk providing details and we will remove access to the work immediately and investigate.

A Review on Functionally Graded Materials and Structures via Additive Manufacturing: From Multi-Scale Design to Versatile Functional Properties

Yan Li,* Zuying Feng, Liang Hao, Lijing Huang, Chenxing Xin, Yushen Wang, Emiliano Bilotti, Khamis Essa, Han Zhang, Zheng Li, Feifei Yan, and Ton Peijs*

Functionally graded materials (FGMs) and functionally graded structures (FGSs) are special types of advanced composites with peculiar features and advantages. This article reviews the design criteria of functionally graded additive manufacturing (FGAM), which is capable of fabricating gradient components with versatile functional properties. Conventional geometrical-based design concepts have limited potential for FGAM and multi-scale design concepts (from geometrical patterning to microstructural design) are needed to develop gradient components with specific graded properties at different locations. FGMs and FGSs are of great interest to a larger range of industrial sectors and applications including aerospace, automotive, biomedical implants, optoelectronic devices, energy absorbing structures, geological models, and heat exchangers. This review presents an overview of various fabrication ideas and suggestions for future research in terms of design and creation of FGMs and FGSs, benefiting a wide variety of scientific fields.

structures of bone or local tissue variation in seashells (e.g., pearl oyster, *Cypraea rufa*, and *Peristernia incarnate*) and plants (e.g., Norway spruce and bamboo).^[3–5] Niino et al.^[6] first proposed the concept of manufacturing a thermally graded metal-to-ceramic phase for a thermal barrier application and FGMs have been intensively investigated since then. In contrast to isotropic bulk materials, the compositions and structures of FGMs can be accurately designed to create tailored multifunctional properties. As a result, FGMs are of great interest for numerous applications, including aerospace engineering, nuclear power generation, sensors, biomedical implants, optoelectronic devices, and energy absorption systems.^[7–12]

1. Introduction

Functionally graded materials (FGMs) are novel composite materials with gradual variations in their compositions and structures throughout their volume and hence locally tailored properties.^[1,2] Many FGMs are commonly found in nature (Figure 1) with examples such as the varying spongy trabecular

Additive manufacturing (AM), also termed as 3D printing, is a near net shape manufacturing process, which can be used to directly manufacture complicated 3D objects without requiring molds, tooling or the need for joining or assembling.^[13] In addition, AM has the advantage of allowing flexible designs which can be optimized for specific geometrical requirements or applications where complex procedures or geometries are too

Dr. Y. Li, Prof. L. Hao, C. Xin, Y. Wang, Dr. Z. Li
Gemological Institute
China University of Geosciences
Wuhan 430074, P. R. China
E-mail: yanli@cug.edu.cn

Z. Feng
School of Biomedical Engineering and Med-X Research Institute
Shanghai Jiao Tong University
Shanghai 200030, P. R. China

L. Huang
School of Mechanical and Automotive Engineering
South China University of Technology
Guangzhou 510640, P. R. China

 The ORCID identification number(s) for the author(s) of this article can be found under <https://doi.org/10.1002/admt.201900981>.

© 2020 The Authors. Published by WILEY-VCH Verlag GmbH & Co. KGaA, Weinheim. This is an open access article under the terms of the Creative Commons Attribution License, which permits use, distribution and reproduction in any medium, provided the original work is properly cited.

Dr. E. Bilotti, Dr. H. Zhang
School of Engineering Materials Science
Queen Mary University of London
London E1 4NS, UK

Dr. K. Essa
Mechanical Engineering
University of Birmingham
Birmingham B15 2TT, UK

F. Yan
Department of Spine Surgery and Musculoskeletal Tumor
Zhongnan Hospital of Wuhan University
Wuhan 430074, P. R. China

Prof. T. Peijs
WMG
Materials Engineering Centre
University of Warwick
Coventry CV4 7AL, UK
E-mail: T.Peijs@warwick.ac.uk

DOI: 10.1002/admt.201900981

time-consuming, expensive, or difficult to manufacture by conventional manufacturing (CM) processes. Currently, the rapid development of AM technologies is no longer restricted to single-phase materials. The capacity to create multi-phase materials with gradual variations in compositions and structures, defined as functionally graded additive manufacturing (FGAM), is already a reality. It represents a layer by layer fabrication that can gradually alter the material composition and organization within a component in order to obtain the desired functionality.^[2] FGAM can involve three types of materials: a) single-phase materials with gradual variations in density like, for instance, in cellular functionally graded structures (FGSs); b) two or multi-phase materials, with gradual variations in material compositions; and c) combinations of these (i.e., with gradual variations of both density and material composition).

Through spatial variation of density and composition, the introduction of functionally graded materials via additive manufacturing (FGMAM) allows the production of versatile FGMs with multiple functions (such as graded mechanical/thermal/magnetic/energy absorbing properties) that are currently inaccessible via CM processes. Generally, the workflow of FGAM involves several steps, including modeling (geometrical modeling, materials modeling and microstructural design), slicing, simulation, manufacturing, in situ characterization, and performance analysis (Figure 2). However, there are still numerous challenges in each stage of FGAM technologies. For example, due to the high incidence of internal/external defects and poor dimensional control, it is difficult to regulate operational variables. Besides, the quality and surface finish standard of fabricated parts can vary greatly between different batches or types of machines.^[14] The delivery speed, accuracy and effectiveness of swapping materials between layers must be continuously improved to fabricate FGAM components with sophisticated internal structures and precision delivery of compositions at the nano/microstructural level.^[15] Right now, commercially available AM technologies still predominantly use homogeneous compositions, that is, a simple geometrical description and the use of single-material FGAM throughout the entire component, as opposed to a multi-material FGAM with heterogeneous compositions. Other limiting factors are the need for high precision in situ techniques for the characterization of such FGAM materials, processes and products,^[14] for example, in situ and real-time monitoring of AM using acoustic emission (AE), real-time detection with machine learning approaches, in situ synchrotron XRD during the laser melting and solidification of alloys, and high speed camera imaging.^[16–18] Moreover, the use of conventional design methodologies restricts the ability to creatively exploit the full capabilities of FGAM. Although an established modeling framework for variable property gradient printing exists, there still remains a need to develop procedures and protocols that achieve more reliable and predictable product outcomes, especially with respect to the distributions of materials with constituent phases and variable properties throughout fabricated structures,^[19] as well as considerations regarding material selection, platform structures, and printing speeds to support FGAM in an economical and environmentally friendly way.^[20] Hence, novel material delivery systems must be developed for the realization of FGAM parts.



Yan Li is an associate professor at the China University of Geosciences, Wuhan. She received her Ph.D from Queen Mary, University of London. Her current research interests focus on material characterization, precious metal alloys, and micro/nano composites additive manufacturing (AM), in particular selective laser melting (SLM), for wearable applications.



Zuying Feng is pursuing her Master's degree in the Department of Biomedical Engineering at Shanghai Jiao Tong University. She received her B.E. degree from the China University of Geosciences, Wuhan. Her research interests focus on graphene reinforced composites via additive manufacturing.



Ton Peijs is a professor at the University of Warwick and director of the National Polymer Processing Centre at WMG. His research focuses mainly on materials and processing innovations in polymers and composites. He received his Ph.D. from Eindhoven University of Technology in the Netherlands and was previously the Professor of Polymer Technology at Queen Mary University of London.

This review elaborates on multi-scale FGAM design concepts, forms and principles of gradients (from geometrical patterning to microstructural design) and summarizes a state-of-art of FGAM technologies with comparison to CM. It also provides an overview of the multifunctional properties achieved together with potential applications in biomedical implants, optoelectronic devices, energy absorbing structures, geological models, and heat exchangers. However, it should be emphasized that many of the examples discussed in this work are still at the research stage. Although FGAM has great potential, real commercial applications are still very few and far between.

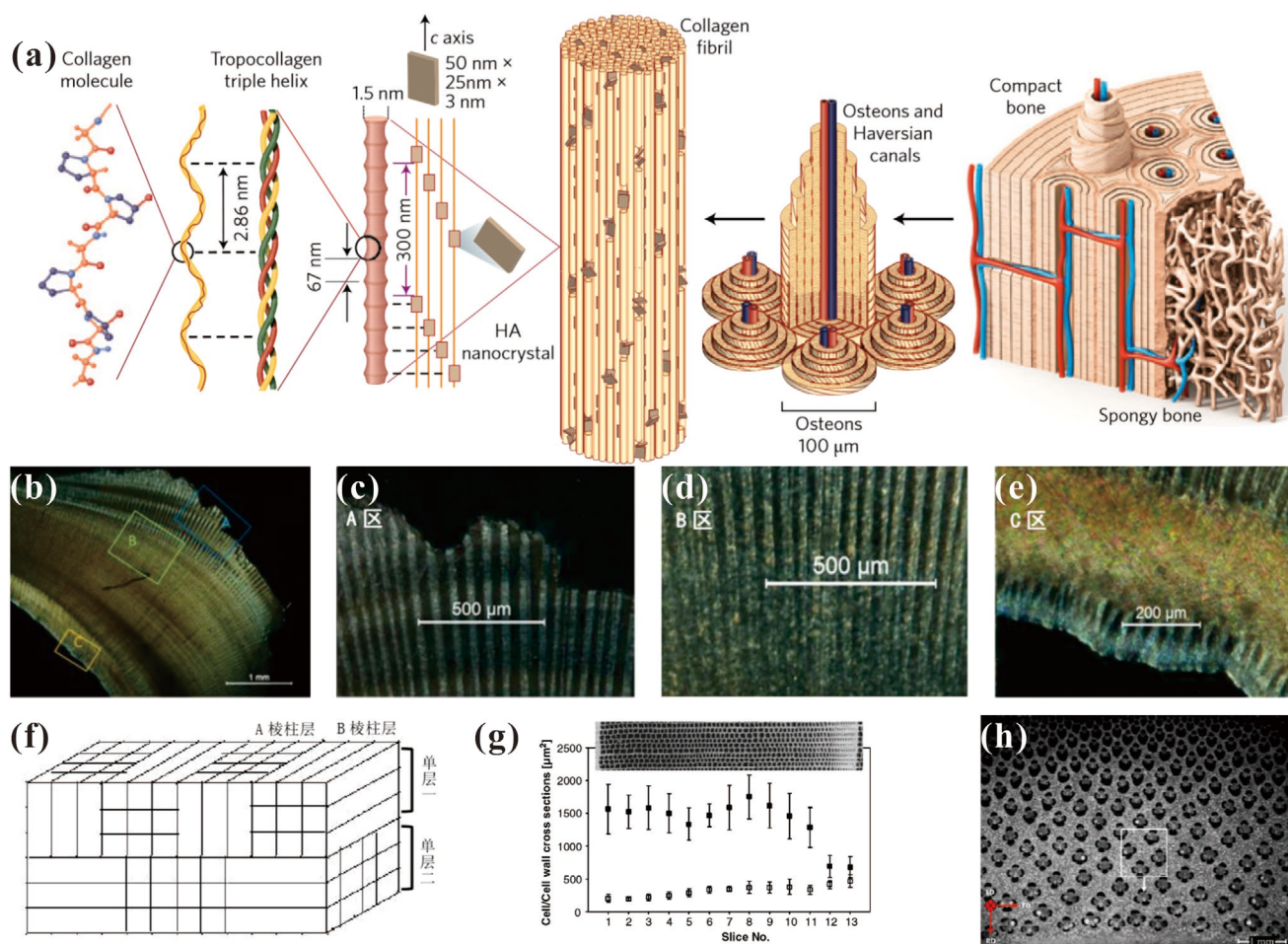


Figure 1. a) Hierarchical structures and gradients of bone: macroscopically, bone displays non-uniform variations in mineral-to-collagen and phosphate-to-carbonate ratios along its length. There is also a gradient of increasing density in the radial direction from the interior spongy (trabecular) bone to the exterior compact (cortical) bone. Reproduced with permission.^[3] Copyright 2014, Springer Nature. The structure of *Cypraea rufa* (a special type of seashell) by polarized optical microscopy: b) arc-shaped parallel layers with uniform distributions of brown organic matter in the slice of *C. rufa* sample. c) Increased magnification of area A in (b). d) Increased magnification of area B in (b), 200 \times . e) Increased magnification of area C in (b). f) Theoretical model of the shell of *C. rufa*. g) Dimensions of cell (black rectangles) and cell wall (white rectangles) cross-sections of Norway spruce across the growth ring. Reproduced with permission.^[4] Copyright 2015, Elsevier. h) Optical microscopy images of bamboo culm with different constituents representing the functionally graded hierarchical structure of bamboo. Reproduced with permission.^[5] Copyright, 2008 Springer Nature.

2. Design Concepts for FGAM

Functional gradients encompass distributed site-specific properties with gradual transitions in geometry, chemical compositions, constituents or microstructures.^[22] The AM workflow consists of a geometrical representation using computer-aided design (CAD), slicing, conversion to the standard tessellation language (STL) file format, support generation, fabrication, and post-processing, which still remain the same as that introduced 30 years ago.^[23] Considering the characteristic of the .STL file format used for 3D printing, data must first be transformed into a boundary representation (B-Rep), resulting in computational overhead, alteration of data, and sometimes even loss of information. In addition, a lack of guidelines on the selection and distribution of materials have also hindered the development of FGAM, thereby limiting the microstructural design and arrangement of transition phases. Although some commercial software packages exist for FGMs

and multi-materials 3D printing, such as the voxel-based systems Autodesk Monolith and Grab CAD, only some basic physical property variations (graded color, transparency, and stiffness) are available, and which are still far removed from real industrial applications and the ever-increasing demands of novel functionally graded components.

Nowadays, AM technologies have already evolved to accurately manufacture complex objects. FGAM research is, however, still in its infancy, a little or nothing has been transferred from basic research to high technology readiness levels (TRL). Especially the way these FGAM parts are designed and the lack of simulation tools available for such complex materials hampers their uptake by industry. Although simulation tools are becoming available for AM,^[24,25] often these tools are not available for FGAM. There are a few examples of successful and/or useful cases, however, many challenges still remain, such as the limited general understanding of advanced multi-material systems, lack of trustworthiness of the process as well as

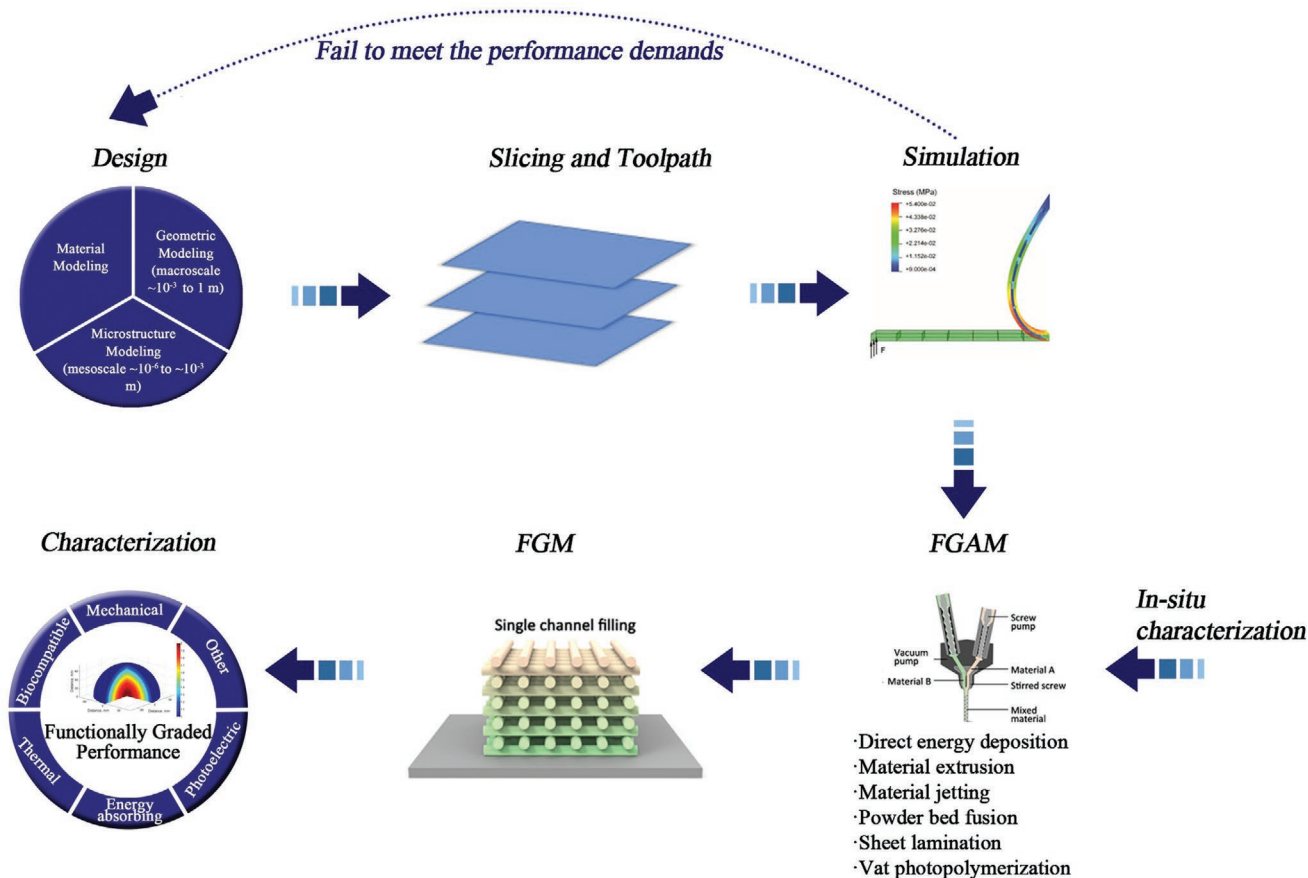


Figure 2. Schematic of FGAM workflow. Reproduced with permission.^[21] Copyright 2020, Elsevier.

uncertainties around final mechanical properties, all of which leading to high overall costs.

Understanding the FGMs design criteria is crucial to obtain versatile functional properties. FGAM places a high priority on the description and assignment of material properties and the behavior of every voxel (the smallest unit in a 3D volume) in the final designed component. The gap between digital design techniques and physical materials-based fabrication tools exists due to the weakness of conventional virtual geometrical-based design systems and shortcomings in the integration of material properties in the design workflow. Therefore, there is a requirement for designers and engineers to communicate with each other and better understand the materials science aspects of their design concepts in order to fully leverage the capabilities of FGAM.

In this section, first, we will focus on the design principles of FGAM, including geometrical representation, material distribution, and the design of graded microstructures. Then, we briefly introduce the simulation methods essential for predicting FGAM performance and providing reliable guidelines for the reconstruction of predesigned models.

2.1. Geometrical Attributes

Geometrical representation is the most fundamental step in the physical visualization of FGMs. FGMs with tailored structural

strengths can be acquired by AM using lattice designs. In addition, a high strength-to-weight ratio is required for lightweight structures or objects. There are four main geometrical representation schemes in conventional CAD tools, including B-rep, function representation (F-rep), constructive solid geometry, and spatial decomposition.^[26] As with the geometrical representation, conventional CAD methods have relatively poor capabilities in terms of representing FGMs and lattice structures. Geometrical representations of 3D objects in B-rep and F-rep, cannot exactly describe the internal structure and material composition of the component, whereas this information is essential for FGMs.

Hence, more computationally efficient and geometrically flexible methodologies of designing FGM models are urgently needed. The following section summarizes three novel geometrical representation methods for FGAM, including reverse imaging modeling, topology optimization (TO), and voxel-based methods.

2.1.1. Reverse Imaging Modeling

Computed tomography (CT) scanning and magnetic resonance imaging (MRI) are image-based methods widely used to assist in the fabrication of patient-specific implants.^[27,28] Reverse imaging modeling is a process that directly interprets 3D structures from CT or MRI data. 2D projections from CT and MRI are utilized to reconstruct the 3D voxel density

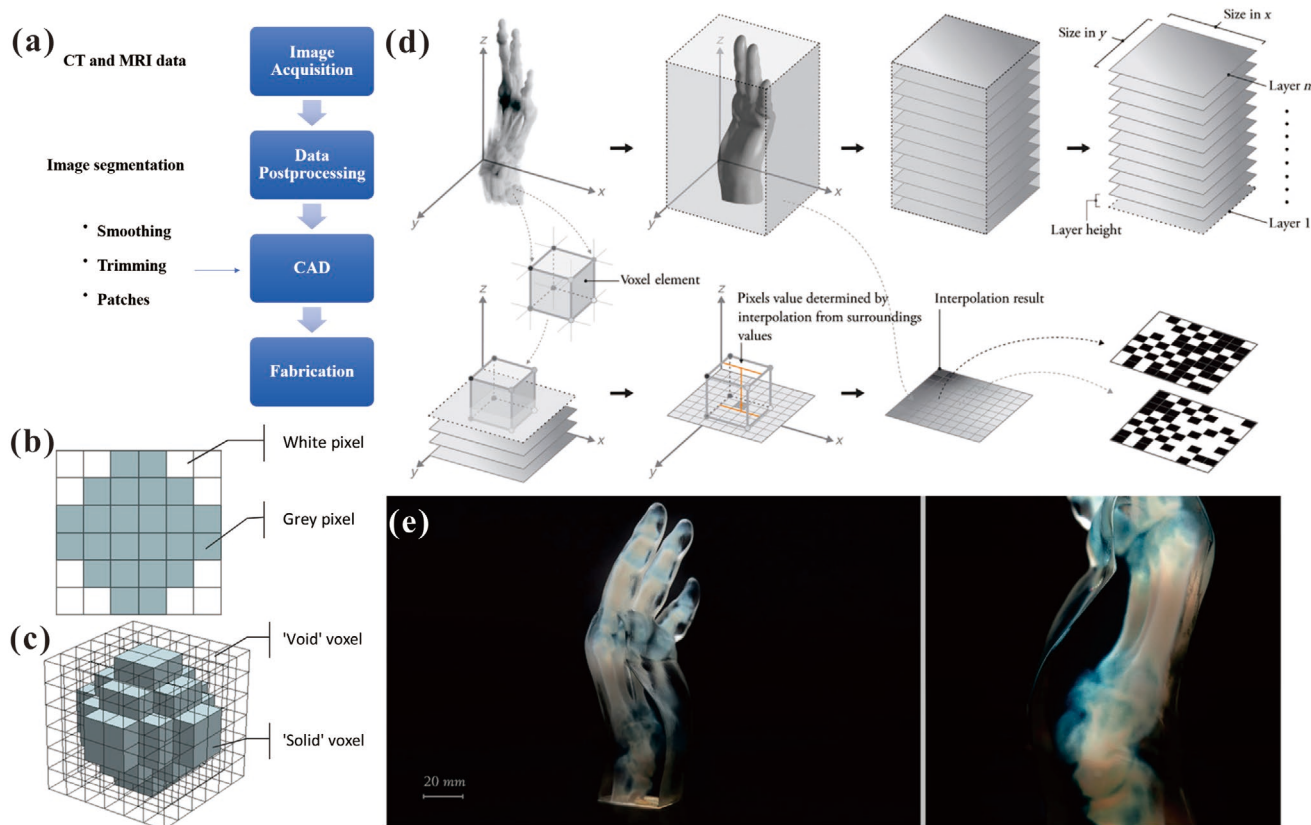


Figure 3. a) AM workflow using CT and MRI data for FGM. b) A 2D pixel image and c) A 3D voxel model. Reproduced with permission.^[54] Copyright 2017, Elsevier. d) Volumetric data-processing workflow and representative 3D-printed models from volumetric data sets. e) 3D-printed model from volumetric data sets from a CT scan of the left hand of a patient with arthritis. Reproduced with permission.^[23] Copyright 2018, American Association for the Advancement of Science.

distribution using algorithms (e.g., a filtered back projection algorithm).^[29,30] Unlike 3D common scanning methods that only obtain surface information, CT and MRI are rapid non-destructive testing (NDT) methods used to interrogate internal structures. In view of CT and MRI technologies, AM design and manufacturing time can be effectively reduced, especially for certain sophisticated FGSs inspired by nature.^[23] AM workflow using CT and MRI encompasses four procedures (**Figure 3a**): i) image acquisition, ii) data post-processing, iii) CAD to design virtual constructs, and iv) AM fabrication of the object. Typically, data from these radiological imaging workstations are stored in a digital imaging and communications in medicine (DICOM) format. To be identified by the 3D printer, the DICOM file format must be converted into STL format. During this process, the most important step is image segmentation, which is utilized to delineate images into regions of interest.^[31] Then, further refinements of the generated CAD are usually required (i.e., wrapping, smoothing, trimming, or adding connectors). The resolution of the CT and MRI data will determine the quality of the reconstructed model. Data with high resolution can be accurately partitioned, resulting in cumbersome post-processing. It is worth noting that the MRI process reconstructs images at a relatively lower resolution, which limits the precision or detail of internal structures (e.g., standard MRI cardiac sequences acquire images with minimal motion, while

it provides slabs of approximately 10 mm thickness and inadequate detail of intracardiac anatomy).^[32] However, nowadays CT images can be reconstructed with slabs as thin as 1 mm, providing higher resolutions for subsequent processing steps.^[33]

2.1.2. Topology Optimization

Topology optimization (TO) has been applied to mathematical algorithms with given external loading, boundary conditions, and constraints to optimize pre-designed material distribution and maximize the performance of as-produced 3D objects. Various algorithms have been implemented in TO to determine the material distribution in a given design domain, including homogenization,^[34,35] solid isotropic materials with penalization,^[36–38] level-set methods,^[39–41] and bidirectional evolutionary structural optimization.^[42,43] The structures selected from commercial software under a given volume fraction or reconstructed from CT images inspired by functionally graded natural objects may attribute a regular or random pattern to the internal FGM structures. When using such algorithms, AM with exquisite details can alleviate limitations in mesh resolution, manufacturing constraints, and post-processing.

Recently, numerous studies have combined TO with FGAM to optimize material distributions for better functional

graded performance.^[44–48] Li et al.^[45] established a scaling law modified algorithm to optimize the stiffness of functionally graded gyroid lattice structures for the fabrication of AM parts. Wang et al.^[46] utilized a reduced-order model to down-scale homogeneous equations, improving computational and design efficiency. Results of simulations and experimental data demonstrated a topology optimized lattice structure with better stiffness than that of a uniform lattice structure. Liu et al.^[47] designed eight unit cells using the TO methodology for printing by stereolithography (SLA). Tailored performance was obtained by a grey level distribution-based design strategy according to the mechanical criterion of unit cells including mechanical anisotropy, plasticity, damage, and densification. Cheng et al.^[48] applied the asymptotic homogenization method to optimize graded lattice structures with predictable mechanical performance. A modified Hill's yield criterion was used to describe the graded lattice structure, whose elastic/plastic properties were better than those of a uniform structure. Latest research has shown that it is possible to simultaneously optimize a macroscopic structure and the lattice distribution inside the structure, by conducting parameterization of the macrostructure in combination with a density-based lattice model.^[49] The addition of spatial variables can solve complex design problems, for example, highly nonlinear mechanical events.^[50]

TO technique exploits the far-reaching capabilities of AM technologies to fabricate sophisticated FGSs like selective laser melting (SLM).^[51,52] However, material extrusion-based AM technologies such as fused deposition modeling (FDM) tend to produce material gradients over the material compositions. In addition, these methods rarely use TO to optimize complex models except for some simple cubic architectures.^[47,53]

2.1.3. Voxel-Based Methods

A voxel, as for volumetric pixel, is analogous to the rectangular pixel that represent a 2D image such as a bitmap. A voxel is the smallest unit in a 3D volume that assumes a logical value with one indicating solid space and zero indicating void space (Figure 3b,c). Unlike the surface representation method in most mesh-based CAD tools, the voxel-based design method can accommodate heterogeneous material properties in order to tailor designs to graded structures. Conventional CAD systems distribute materials based on existing geometries, whereas voxel-based methods can design material compositions and geometrical coordinates separately. Voxel representation schemes can be used to embed a vast range of lattice topologies in complex 3D objects. However, this strategy may exceed the modeling capabilities of current CAD systems. Fine voxel sizes can improve the detailed modeling, albeit at the expense of increased computational time and costs. An appropriate choice of the size and resolution of a voxel should therefore be used to achieve reasonable computational precision at acceptable costs.

Voxel-based representation schemes have been applied to FGAM. Aremu et al.^[54] proposed a novel, voxel-based method to represent lattice structures comprised of an arbitrary external geometry and any lattice cell. In addition, the voxel-based method has been utilized to generate FGSs by overlaying a grayscale image onto a predesigned voxelized domain.

Liu et al.^[55] integrated a voxel-based scheme with ANSYS parametric design language to simultaneously design and simulate the properties of FGMs. One successful commercial development was provided by Stratasys Ltd., a leading manufacturer of 3D printers who developed a multi-material voxel 3D printer with the voxel-based modeling engine GrabCAD Print. Unlike traditional surface representations that may lead to information loss, the voxel-based method can directly translate geometrical models into a rasterized description that can be used in a voxel 3D printer to produce FGMs. This multi-material 3D printing is a PolyJet AM method that simultaneously deposits several different photopolymer droplets layer-by-layer to construct 3D FGM objects with graded color, transparency, and stiffness. Using the Connex 3D printer of Stratasys Ltd., Drobowski et al.^[56] fabricated a prosthetic socket with multifunctional properties at the voxel level. In addition, Bader et al.^[23] proposed an approach for directly manufactured numerous data sets (e.g., unconnected point cloud data, lines and curves, open surfaces, and volumetric data, Figure 3d,e) into physical entities using voxel-based 3D printing, which was proved to be a potential tool for scientific visualization. It is also interesting to note that the development of voxel design has been closely related to 4D printing (3D-printed components that can change shape once exposed to specific environmental conditions, such as temperature, light, or humidity. The fourth dimension is a transformation over time with the ability to autonomously change form^[57]). Materials involved has already included piezoelectric, electrical, magnetic, and photostrictive materials as well as transformer hydrogels.^[58]

Voxel-based printing is of great interest to FGMs, but some challenges still need to be considered. A database for material distribution should be set in advance, which needs extensive experimentation. Designers now are required to master the geometrical modeling method as well as understand the materials science aspects of the to be printed parts (e.g., material compositions, structures, properties, and performance).

2.2. Materials Attributes

The multi-material distribution in FGMs removes distinct boundaries, hence avoiding delamination and/or cracks due to discrete changes in material compositions and properties, and achieving multifunctional properties. Although most designers are familiar with the modeling of complex geometries, they may lack of experience using virtual software to design non-geometrical parameters (i.e., material properties, reactions, and compatibility). Duro-Royo and Oxman^[59] presented a fabrication information modeling (FIM) approach to stress the importance of providing information regarding geometries and material properties across length scales and disciplines. The following sections provide a brief description of existing design methodologies for material compositions.

2.2.1. Materials Compositions

One conventional CAD system that focuses on the geometrical modeling using homogeneous materials is 3D Euclidean space

E^3 . The distribution of materials can be considered as an additional dimension by using a unit vector to represent the FGM model. In addition to a geometrical representation, FGM object modeling also requires material heterogeneity to be defined over the geometrical domain. When a design combines both geometrical and material information, the modeling space expands to a fiber bundle $E^3 \times E^k$, where the geometry space E^3 is the base space, material space E^k is the fiber space, and k ($k \geq 1$) is the number of primary materials under investigation. If one only considers material composition, the composition of FGMs at a point X is described by a vector.^[54] Based on both the geometrical and material attributes, FGM based solid objects can be represented as:

$$X = (X_g, X_m) \quad (1)$$

$$X_g = (x, y, z) \in \Omega_g \subset E^3 \quad (2)$$

$$X_m = (r_1, r_2, \dots, r_k) \in \Omega_m \subset E^k, 0 \leq r_i \leq 1 \quad (3)$$

$$1 \leq i \leq k, \sum_{i=1}^k r_k = 1 \quad (4)$$

where X_g is the location of a point X in the geometrical domain Ω_g , X_m is the material composition defined at X_g , and Ω_m is the material domain (subspace of E^k). The scalar r_i in the vector (r_1, r_2, \dots, r_k) represents the volume fraction of the i th primary material, the sum value of all the scalars should be one such that the material composition X_m is physically meaningful.^[60]

2.2.2. Materials Distributions

Numerous solutions have been evaluated to represent different types of FGM objects. Chiu et al.^[61] proposed a multi-material tree structure to store material information from which the homogeneous material region can be directly extracted. This structure enables the representation and fabrication of heterogeneous materials via AM. Kou and Tan^[62] classified the representations of heterogeneous objects into two categories, evaluated and unevaluated models according to model precision and compactness. Through intensive space decompositions, evaluated models can represent heterogeneous material distributions in an inexact and discrete form, including voxel and volume mesh-based models. In contrast, unevaluated models such as the explicit function model, control feature model, control point model, and the implicit function model do not rely on intensive spatial decomposition, subdivision, or discretization. By applying accurate geometrical data representations (e.g., B-Rep or F-Rep) as well as rigorous functions to represent the material distributions (explicit, implicit, analytic, or procedural), unevaluated models provide sufficient fidelity in geometries and material distributions. Zhang et al.^[63] divided the modeling of FGM objects into three categories. The first category is conventional geometrical representation based FGM modeling, which addresses material distributions by extending conventional geometrical modeling. This modeling restricts

the modeling capacity of irregular and compound materials that vary throughout the geometrical structure. Another approach is geometry independent FGM object modeling by configuring material composition independent from geometrical information. This method can define highly complex geometries and sophisticated material distributions, but it is unfavorable in capturing designers' intentions since material configuration strongly depends on the coordinate system. The last approach is a new FGM modeling approach that uses simple material primitives, that is, points, 1D curves (straight lines or splines), and planes to build sophisticated material distributions (Figure 4a–d). Gupta et al.^[60] investigated a material convolution surface-based approach using material primitives. Through the use of various 1D material distributions model by membership functions and material potential functions, 2D and 3D material distributions (Figure 4e,f) can be generated for irregular heterogeneous objects.^[60]

When defining an appropriate material distribution function, the intended material composition can be mapped over a 3D space. Bhashyam et al.^[64] summarized a library of material composition functions, and designers can choose a function appropriate for the intended FGM applications. Realization of compositional gradients is depending on a computer program by controlling the mixing ratios of multi-materials during their deposition. It is believed that pre-mixing two or more raw materials is beyond the scope of FGAM.^[65] However, to create a computer database of multifunctional properties in accordance with material-mixing ratios is not always easy. By producing a series of exemplary specimens with designed material compositions and measured material properties matching with material-mixing ratios, Bader et al.^[23] constructed a material information database for multi-material 3D printing. However, the results showed a nonlinear relationship between mixing ratios and material transparency; thus, a linear variation in mixing ratio distribution did not yield a linear variation in graded material properties. Designers must therefore develop solutions to non-uniform mixing ratios and graded material properties.

2.3. Microstructural Attributes

Apart from geometrical and material attributes, the microstructure is another important factor for determining physical properties (e.g., hardness, tensile strength, fracture toughness, thermal expansion, magnetism) of the FGMs. Knowledge of the microstructural morphology and distribution is needed to fully explore the potential of FGAM.^[66–71] The process parameters when operating AM techniques (e.g., laser energy, beam size, deposition rate, process temperature, scanning strategy, and materials composition), especially those of high energy, have an obvious effect on the microstructure of 3D object. Most of these factors affect the thermal gradient and the velocity of the solidification and can lead to differences in crystalline growth and grain size, grain refinement, orientation, structure as well as morphology, thus affecting the final properties of the component. Previous research has shown that the higher deposition rates lead to a larger melt pool and higher scanning velocity and as a result an increase in the proportion of equiaxed grains (Figure 5a).^[72] Our research team previously demonstrated that

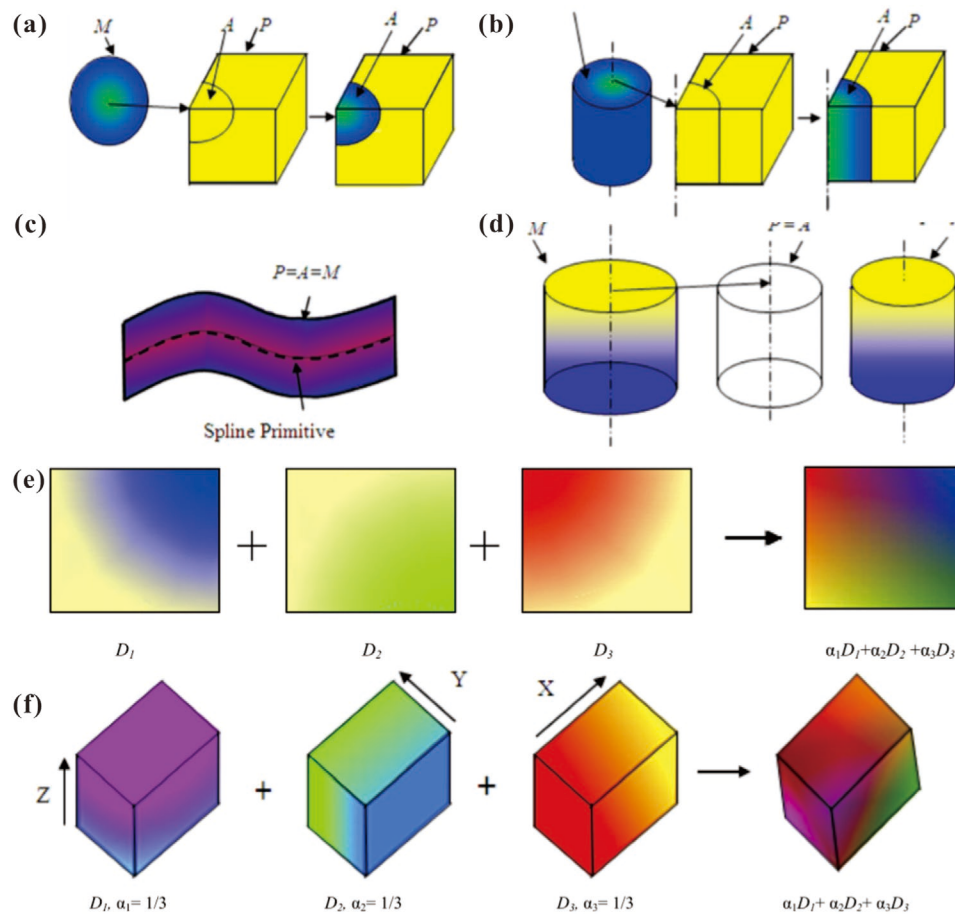


Figure 4. Material modeling with convolution surface-based material primitives: a) Point; b) Straight line; c) Spline; and d) Plane. e) 2D material distribution in an object obtained by merging three 1D material distributions. f) 3D material distribution in an object. Reproduced with permission.^[60] Copyright 2015 Elsevier.

the grain size of silver alloys can be controlled by adjusting laser parameters. A fine equiaxed grain ($0.40 \mu\text{m}$) is formed when applying a low laser energy density (41.6 J mm^{-3}), resulting in an increase in hardness of the silver alloy specimens by up to 200% compared to those manufactured by a casting process.^[73]

Grain size is proportional to the height of the deposited layer of a 3D printed object; in other words, as the deposited height increases, the thermal gradient also increases (Figure 5b).^[74] The β phase of Ti-6Al-4 V alloy can increase with building thickness because a higher cooling rate and temperature profile increase the growth rate of martensite along the AM direction.^[74,75] In addition, a thermal gradient has also been found to impact the crystalline texture of grains because of different scanning strategies.^[76,77] The atmosphere present in the building environment might be affected by the printing, thus leading to a change in its microstructure. Impurities caused by inert gas being re-deposited onto the scanned area can result in a porous part.^[78] Besides, AM defects (e.g., pores, rough surfaces, and lack of a fusion between layer) and other factors may also influence the microstructure. Material composition is certainly a key factor that affects the microstructure of the products. Wang et al.^[66] fabricated a functionally graded Ti-Al alloy using a double-wire arc AM method by varying the wire feeding speed and the Ti and Al concentrations. With increasing Al

concentration (vertically from bottom to top), a graded phase pattern of $\alpha + \beta \rightarrow \alpha + \alpha_2 \rightarrow \alpha_2 \rightarrow \alpha_2 + \gamma \rightarrow \gamma$ was observed in microhardness (Figure 5d), and tensile strength increased to a maximum and subsequently decreased due to changes in phase composition and grain size.

A microstructural representation can be obtained from experimental measurements or simulations of microstructural evolution. Microstructural meshes can be generated from electron backscatter diffraction data, and through the use of the open-source code DREAM3D, a statistically equivalent representation of a representative volume element (RVE) of the microstructure can be generated. By using binary, ternary, or quaternary phase diagrams, the desired graded microstructural phases (Figure 5c) can be obtained through predictive phase diagram modeling.^[71,79] Calculation of phase diagrams (CALPHAD) based thermodynamic calculations were implemented to model gradient paths and predict microstructural phase arrangements.^[67,69] Zuback et al.^[80] fabricated transition joints using graded 2.25 Cr-1 Mo steel and Alloy 800 H to prevent carbon diffusion between dissimilar austenitic and ferritic alloys. With the aid of the CALPHAD technique, carbon chemical potentials and martensite transformation temperature for FGMs can be calculated using the General Steel database in JMatPro V8 software, taking the chemical composition as

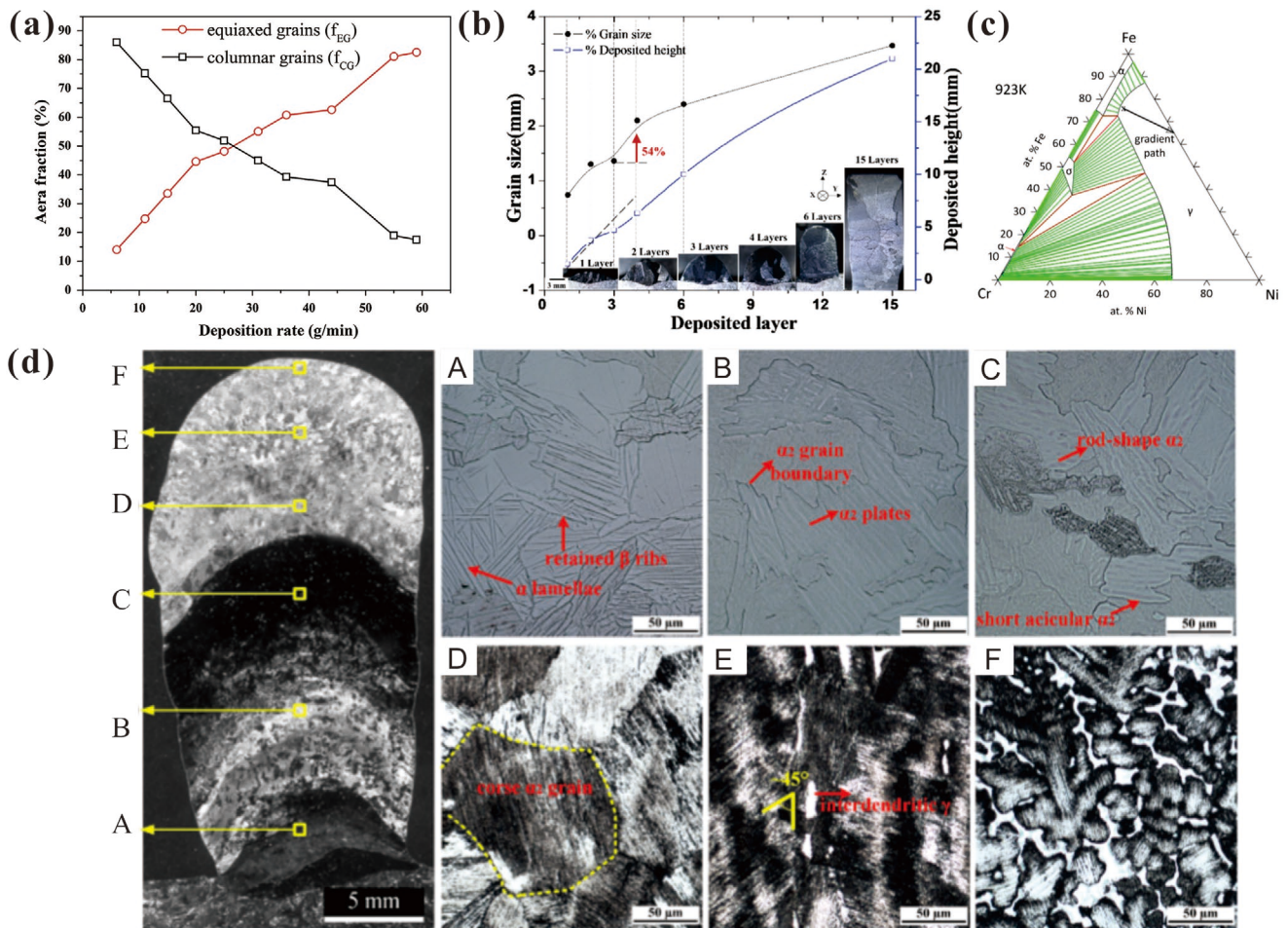


Figure 5. a) Variations in the area fractions of equiaxed and columnar grains as a function of mass deposition rate. Reproduced with permission.^[72] Copyright 2015, Elsevier. b) Evolution of prior β grains and heights of different deposited layers. Reproduced with permission.^[74] Copyright 2018, Elsevier. c) Calculated phase diagram at 923 K showing a “gradient path” from stainless steel 304 L (Fe₆₈Cr₂₀Ni₁₀Mn_{<1}Si_{<1} in wt%) to Invar 36 (Fe₆₄Ni₃₆ in wt%). Reproduced with permission.^[71] Copyright 2014, Springer Nature. d) Images of microstructural evolution with progressively higher Al content from bottom to top. Reproduced with permission.^[66] Copyright 2018, Elsevier.

the input. Moustafa et al.^[81] developed new non-equilibrium phase diagrams, so-called Scheil Ternary Projection diagrams, to optimize the design of Fe-Cr-Al ternary FGMs. Preliminary results revealed that intermetallic phase fields expanded dramatically through rapid solidification during the AM process. In addition, several studies have focused on simulation assisted methods, which will be discussed in the following section, for the prediction of microstructure in AM, including cellular automata-finite elements,^[82,83] cellular automata-lattice Boltzmann,^[84] and Monte Carlo methods.^[85,86] Based on the above research results, despite some methods such as CALPHAD, which have been proposed for the predesign of microstructures of FGM parts, a systematic and powerful commercial design platform is urgently required and still under development to precisely pre-arrange microstructural phases.

2.4. Simulation and Computer-Aided Engineering

Simulation and Computer-aided engineering (CAE) methodologies play a critical role in modeling and optimizing AM design

processes via predicting the as-produced geometry, properties, and functional performance of produced components. Through accurate simulation, physical processes of AM techniques can be examined to quantify how AM process variables affect the resulting components' properties. As a result, tedious experimentation is avoided to reduce the qualification cycle of AM parts. In comparison to general AM techniques, FGM is highly nonuniform and undesirable graded features may occur. This may lead to changes in micro- and/or mesostructural morphologies and uncertain multifunctional properties. Inevitably, a full understanding of the discrepancy between predicted and actual FGM components is required to mitigate defective parts.

To date, the overwhelming majority of research in this area has focused on finite element analysis (FEA) based CAE methods that are widely implemented for macro-scale simulation of thermo-mechanical processing of AM parts (e.g., heat transfer, solidification, deformation).^[87] FEA methods have been widely used to optimize the distribution of graded cellular lattice structures and enhance the strength-to-weight ratio of FGSS.^[45,48,88–90] Geometrical complexity of predesigned 3D

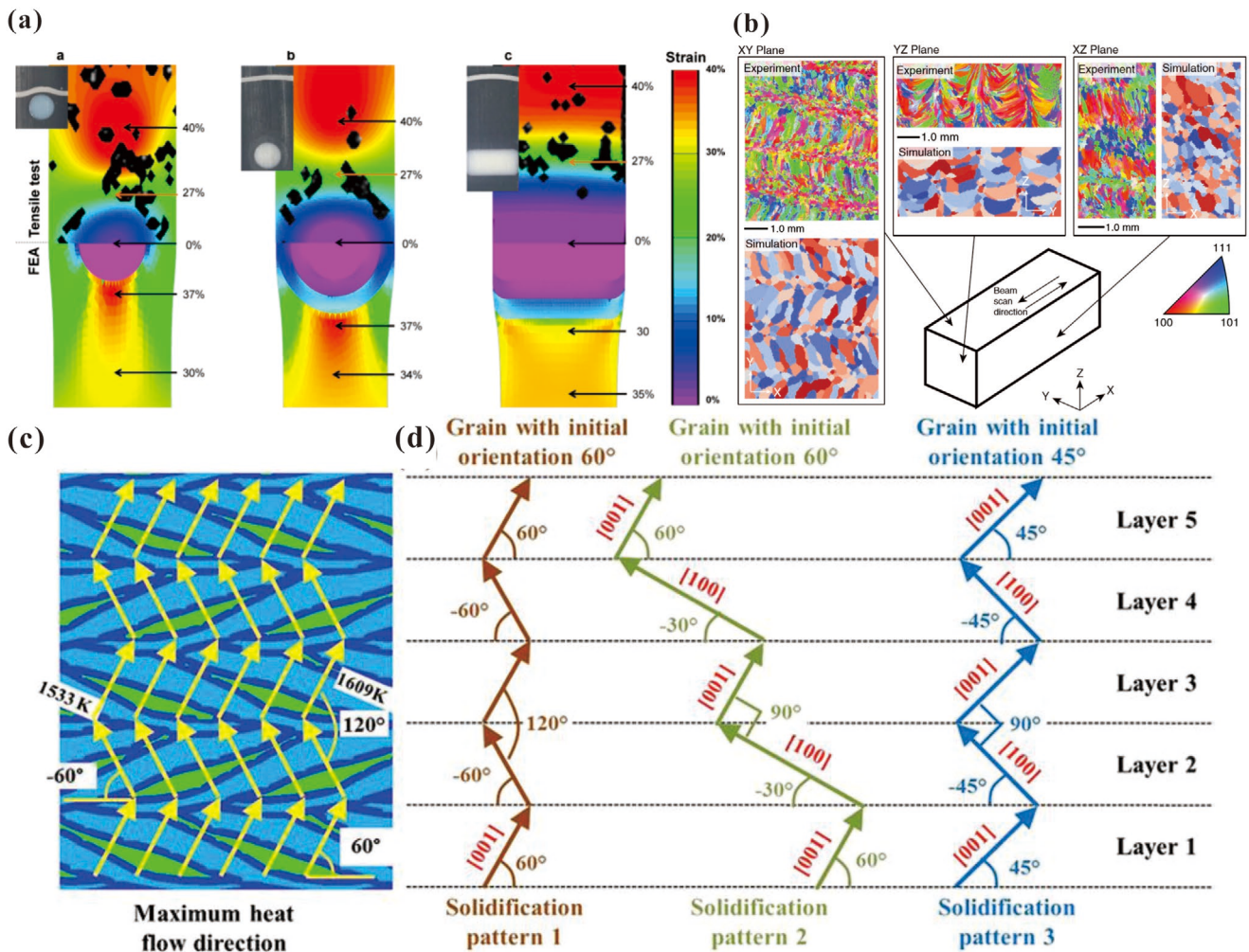


Figure 6. a) Visual comparison of strain distribution according to FEA simulation and physical tensile tests (inset figures: images of failure locations when samples were stretched until breakage). Reproduced with permission.^[91] Copyright 2018, Elsevier. b) Comparison of experimental and simulated microstructures along orthogonal planes in an object fabricated by AM. Reproduced with permission.^[97] Copyright 2017, Elsevier. c) Calculated temperature field with maximum heat-flow directions indicated with yellow vectors. d) Schematic illustration of primary dendritic growth patterns of grains with different orientations during bidirectional laser scanning. Reproduced with permission.^[99] Copyright 2015, Springer Nature.

objects results in a computationally cumbersome discretization procedure at the mesh definition stage in FEA. Parthasarathy et al.^[88] incorporated a RVE method into FEA for simulation of the stiffness of FGs with greatly improved computational efficiency. By virtue of FEA, multifunctional performances of FGMAM, such as by tailoring strain distributions to failure site and a linear gradient modulus, were successfully predicted.^[91–93] FEA based simulation data proved a good match with experimental data of FGMAM (Figure 6a). Latest research confirms a highly efficient simulation approach for nonlinear deformation of soft lattices.^[94]

Computational fluid dynamics (CFD) is used to analyze and predict the motion of fluids, diffusion of species and phase changes, while ensuring mass, momentum and energy conservation through a system of nonlinear partial differential equations. However, detailed numerical simulation using CFD is computationally expensive for complex FGM problems, and therefore a more efficient analysis method is urgently required. FEA simulations were developed to investigate the

thermal trace of laser based AM objects and the prediction of microstructure and properties.^[75,95,96] Rodgers et al.^[97] explored a modified kinetic Monte Carlo Potts model-based simulation method using the shape of the molten zone and surrounding temperature gradient together with a scanning pattern for the modeling of microstructural evolution. This flexible method leads to a reduction in computational time and costs, and simulated microstructures were consistent with experimental data (Figure 6b). An enriched analytic solution model (EASM) was developed by Steuben et al.^[98] for AM simulation. The results of EASM were equivalent to those of FEA, whereas the computational efficiency was roughly six orders of magnitude faster. Wei et al.^[99] used numerical modeling to calculate heat transfer and liquid metal flow in a nickel-based alloy during multi-layer AM process. The evolution of solidification textures under both unidirectional and bidirectional laser scanning patterns was investigated (Figure 6c,d). This provided scientific principles for customizing solidification textures, which influenced the final performance of the product.

Multifunctional performances such as carbon concentration profiles and heat transfer performances can also be simulated for FGMAM.^[80,100]

Clearly, a great number of simulation methods have been investigated to predict various characteristics of components produced by AM at an experimental scale. Nevertheless, Few methods exist that can capture microstructural details across a sufficiently large length scale to predict microstructures over many passes and layers. Hence, there is also an urgent need to integrate modeling and simulation to connect fabrication process with multifunctional performance outcome.

3. Manufacturing Methods for FGMs and FGSs

3.1. Conventional Manufacturing Methods for FGMs and FGSs

The number of publications related to FGMs has increased rapidly since the concept was first proposed by Niino et al.^[6] in 1972 and can be broadly classified into two fields: bulk processing methods and coating methods (Figure 7a).^[101] Table 1 presents a summary of various fabrication techniques for FGMs. Some studies describe bulk processes such as sedimentation, powder stacking, and centrifugal casting. Others describe the coating of surfaces by slurry dipping, chemical solution deposition, and chemical vapor deposition. Some methods sit in between these two categories, such as thermal spraying, laser cladding, and electrophoretic deposition. However, even with one of the most widely accepted and applied CM methods, that is, the thermal barrier coatings, limitations are obvious because they can only construct simple FGM objects with uncomplicated gradient structures.^[92] Due to limitations of CM to manufacture complex shapes and customized multifunctional properties,^[63] the emergence of AM methods offers new opportunities for designers and engineers to manufacture FGMs or FGSs. Recent innovation and rapid technological advancement in FGAM systems offer a future direction to achieve spatial gradients in material compositions and structures. As illustrated in Figure 7b, the

main technological processing differences between CM and AM methods include improved geometrical designs, graded property variations and formed styles. Although FGAM are currently not ready for real industrial applications, the development of more precise spatial material distribution systems and structural morphologies, accompanied by newly developed multiple design tools have been successfully exploited in some preliminary FGAM researches.^[74]

3.2. Additive Manufacturing Methods for FGMs and FGSs

AM methods are a solid freeform manufacturing technology that accurately fabricates FGMs or FGSs to precisely form a pre-designed 3D object. Here we have collected state-of-the-art FGAM cases reported in the literature so far. Based on standard ISO/ASTM 52900,^[131] FGAM methods can be divided into several categories including direct energy deposition (DED), material extrusion, material jetting, powder bed fusion (PBF), sheet lamination, and vat photopolymerization. Although these methods have proven to facilitate the FGAM, they are still in a prototype stage and their potential is not fully explored yet. For instance, comprehensive studies of material availability and material properties are often lacking, yet compulsory for actual applications. Beside, each FGAM process has some limitations and continuous efforts need to be undertaken in order to realize practical applications.

3.2.1. Direct Energy Deposition

DED methods can reinforce, repair, or clad components by melting metallic wires or powders via a focused electron or laser beam. Direct laser metal deposition (DLMD) is an important DED technique that is commonly divided into two main categories according to the materials used: wire arc additive manufacturing (WAAM) and laser metal deposition (LMD). By controlling the individual wire feeding speed, the WAAM

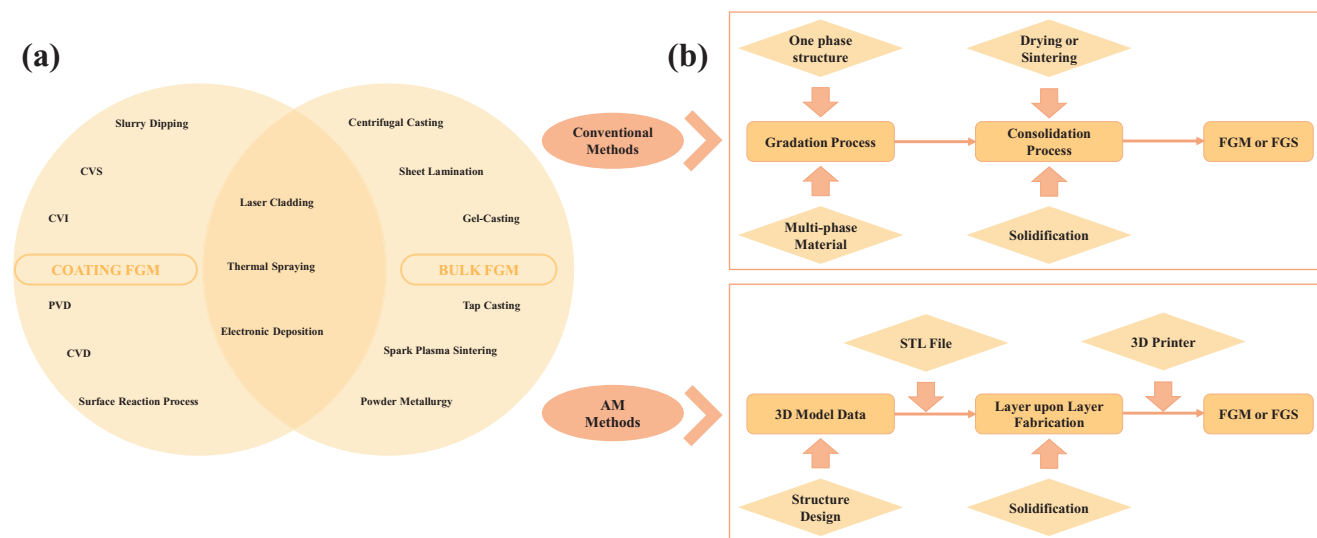


Figure 7. a) Different conventional FGM manufacturing methods. b) Differences between CM and AM methods.

Table 1. A summary of conventional FGM methods.

Classifications	Techniques	Characteristics	Materials	Applications	Refs.
Gas phase processes	Vapor deposition techniques (CVD/CVI/CVS)	Energy intensive, low efficient and uneconomical	SiC/C, TiC/SiC, ZnO TiO ₂ /Ti-O-Si etc.	Optoelectronics and electronics	[102–104]
	Thermal spraying	Optimal technological conditions affected by various parameters	ZrO ₂ /NiCrAlY, Polyimide/WC-Co, CeO ₂ -Y ₂ O ₃ -ZrO ₂ , etc.	Aerospace, military and commercial	[105–109]
	Surface reaction process	Depended on diffusing reactive gases, surface contact reactions	Titanium alloys, WC-Co/Ni, etc.	Surface treatment for metals	[110–112]
Liquid phase processes	Centrifugal casting	Gravitational/centrifugal forces to reinforce the particles,	Metals	Special needs like forging, poor degree of deformability	[113–115]
	Combustion	Productive, energy saving, remarkable recrystallization	TiC-Fe-Al ₂ O ₃ , TiC-Ni, TiC-Cu, etc.	Nanomaterials, ceramic and catalyst industries	[116–119]
	Tape casting	Raw materials control drying and sintering processes	Ceramic powder	Multilayer ceramic substrates	[120,121]
	Gel casting	Time-saving, environmental-friendly, low-cost	Mixed dispersant, monomer, dimer, initiator and catalyst	Ceramic materials	[122,123]
Solid phase processes	Electrophoretic deposition	Simple processes and equipment, little restriction in shape, no binder burnout	ZrO ₂ /Al ₂ O ₃ and WC/Co, HA-TiO ₂ , Ti-6Al-4 V, etc.	Emitter for electrons, ceramic appliances	[124–126]
	Spark plasma sintering	Easy to be activated and purified for powder	ZrB ₂ -SiC/ZrO ₂ , ZrO ₂ and B4C, etc.	Cut/hard/ wear resistance materials, fabrication of glass-lens molds	[127,128]
	Powder metallurgy	Good control of microstructure and composition	Mullite/Mo, hydroxyapatite (HA) -Ti, etc.	Auto industry and equipment manufacturing industry	[129,130]

process (Figure 8a) can use wires made from different metals such as pure titanium and 1080 pure aluminum to manufacture components with a chemical composition gradient.^[66] Analogously, a metallic graded object can be fabricated via LMD through adjusting the volume of powders fed into a melt pool under a moving laser (Figure 8b).^[132]

As DED methods are a fusion-based process, the development of intermetallic phases in the gradient zone can result in potentially undesirable properties during solidification. To solve this problem, Carroll et al.^[68] investigated the characterization and thermodynamic modeling of functionally graded 304L stainless steel/Inconel 625 and determined the feasibility

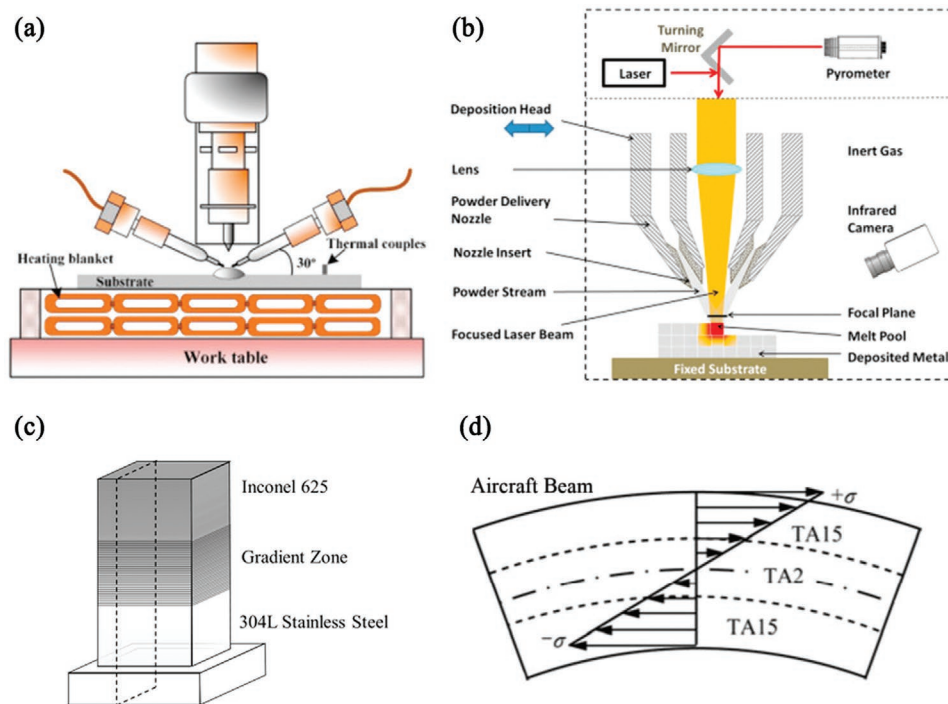


Figure 8. DLMD methods. a) Double-wire feeding process. Reproduced with permission.^[66] Copyright, 2018 Elsevier. b) Metallic powder process. Reproduced with permission.^[132] Copyright 2015, Elsevier. c) Schematic of a graded alloy specimen. Reproduced with permission.^[68] Copyright 2016, Elsevier. d) Schematic of an FGS in an aircraft beam. Reproduced with permission.^[133] Copyright 2014, Elsevier.

of building a graded component without sharp microstructural and/or compositional boundaries. There were approximately 24 layers in the graded zone and the volumetric concentration of each powder altered by 1 vol% (Figure 8c). Qian et al.^[132] also adopted the same deposition method to vary the mass fractions in an aircraft beam (Figure 8d). High strength TA15 (Ti-6.5Al-2Zr-1Mo-1 V) was applied to the highly loaded exterior of the beam, while high ductility TA2 (Grade 3 CP-Ti) was used for the less loaded interior of the beam.

3.2.2. Powder Bed Fusion

Similar to DED technology, PBF also uses lasers to build metal or polymer prototypes, and covers various methods including direct metal laser sintering, electron beam melting (EBM), selective laser sintering (SLS) and SLM. However, rather than using multiple materials and constant laser delivered processes, PBF uses energy density and special structures to achieve functionally graded variations. The powder is selectively melted by a laser beam at specific regions repeatedly, thereby stacking single layer to form the final product (Figure 9a).^[132]

One of the PBF methods that can sinter a large variety of ceramics and polymers is SLS. Chung et al.^[136] investigated the influence of filler volume fractions on nylon-based composites.

A design of experiments (DoE) approach, combining processing parameters and their outputs, was used to design the parameters for each composition. They added 15 nm fumed silica at 0–10 vol% into Nylon-11 to fabricate functionally graded polymer composites. The parameters determined by the DoE were again verified, and final samples showed competitive tensile and compressive mechanical properties.

Similar to SLS, SLM can be used to fabricate porous structures for surgical implants and lightweight automotive and aerospace applications.^[137] Niendorf et al.^[138] employed a two laser SLM system to create graded structures made from 316L powder to fulfill various local functionalities. Maskery et al.^[139] studied the relationship between mechanical behavior and graded density. The same amounts of energy (6.3 and 5.7 MJ m⁻³) were absorbed by the graded and uniform structures, while densification of the graded structures resulted in a 7% lower strain. They proposed that deformation and energy absorption were more accurately predicted in graded density SLM Al-Si10-Mg lattices (density changes with strut diameter, Figure 9b) than that in uniform ones. Choy et al.^[140] used Ti-6Al-4 V powders to fabricate cubic and honeycomb lattice structures with a continuous density change. These FGSs varied linearly from 0.4 to 1.2 mm (Figure 9c). The results suggested that, for a fixed volume, a honeycomb structure can contain more unit cells than a cubic structure, hence

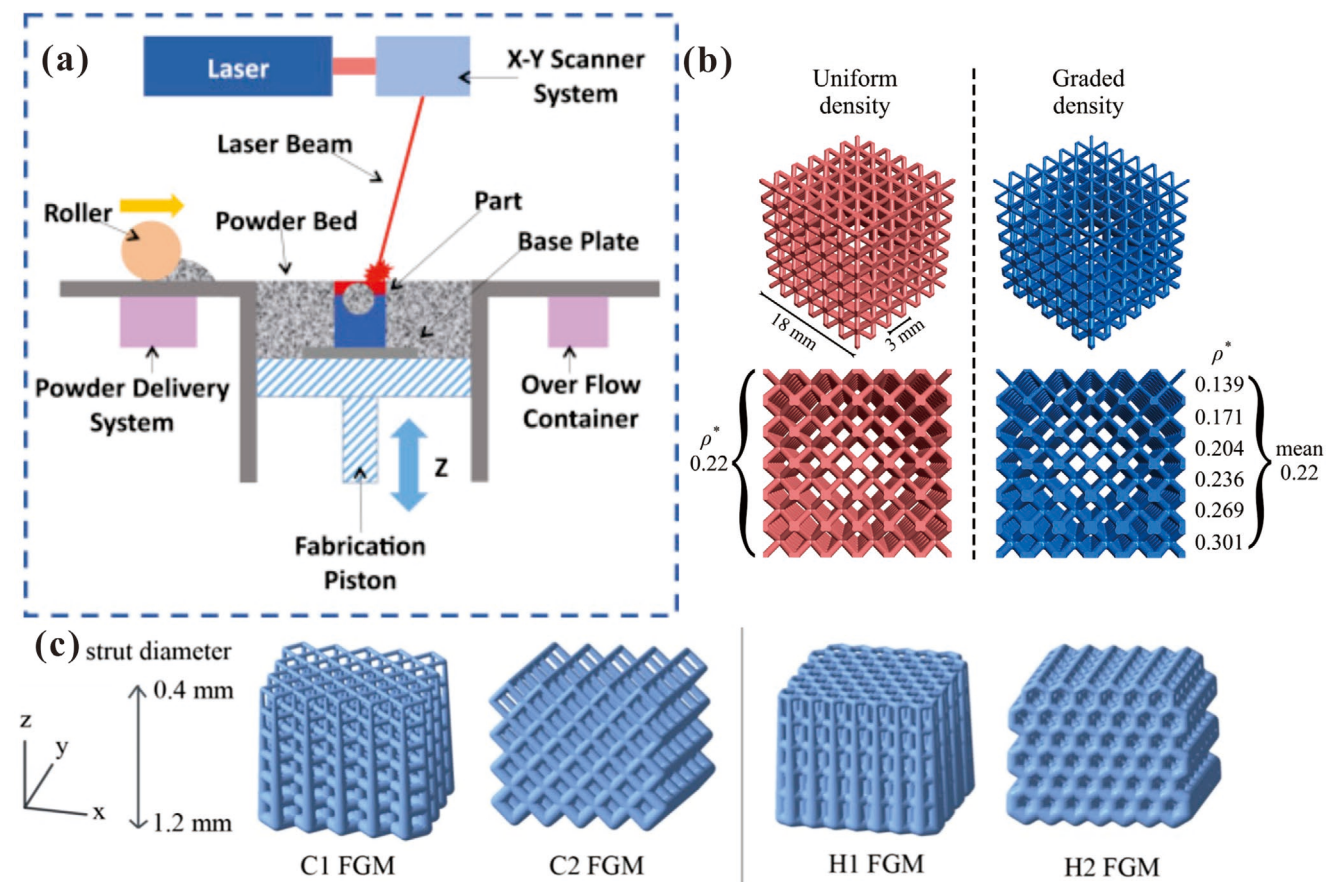


Figure 9. a) The principle PBF process. Reproduced with permission.^[132] Copyright 2015, Elsevier. b) Uniform (left, relative density 0.22) and graded (right, relative mean density 0.22) lattice structures made via SLM. Reproduced with permission.^[140] Copyright 2016, Elsevier. c) Cubic and hexagonal FGS made via SLM. Reproduced with permission.^[139] Copyright 2017, Elsevier.

confirming that FGMs with a honeycomb structure were more space-efficient.

Both two laser-based methods, DED and PBF, can achieve relatively high resolutions, thus obtaining high quality parts. The high laser power induces a thermal gradient, which may affect the microstructural phases and can cause severe cracking as mentioned in Section 2.3, further influencing its performance. However, it is still challenging for these laser-based methods to regulate the cooling and heating rate during the FGAM process.

3.2.3. Sheet Lamination

Sheet lamination processes such as laminated object manufacturing and ultrasonic consolidation (UC) fabricate desired objects by joining different layers and foils. However, these sheet lamination methods may have difficulties in realizing material gradients, and few examples in the literature related to FGAM using sheet lamination are found. Kumar et al.^[141] fabricated functionally graded alloys by joining stainless steel, Cu and Al foils with the assistance of UC. They reported optimal processing parameters to create a minimum sample (size of $33 \times 5 \times 0.64 \text{ cm}^3$) and adjusted these parameters to create metallic FGMs with graded strength in the deposition direction.

3.2.4. Materials Extrusion

The material extrusion method usually uses a single or multiple extruder, each extruding a paste of materials layer-by-layer. A multi-nozzle device allows for the production of arbitrary components by controlling the flow ratio of different pastes. Kokkinis et al.^[92] fabricated an FGM using two different resins (mainly comprising of different amounts of acrylates and methacrylates) by a volumetric two-component dispenser (Figure 10a), with the elastic modulus varying from 0.1 to 319 MPa over the graded region. In another work, Leu et al.^[134] prepared FGMs using a novel material extrusion method called freeze-form extrusion fabrication under the freezing point of water by a triple-extruder mechanism (Figure 10b). The pink and green colored Al_2O_3 and ZrO_2 graded parts in the figure were built by changing the relative flow rates of the corresponding plungers.

Fabrication of FGMs with linearly varying properties is ubiquitous for a wide range of material extrusion techniques. Bakarich et al.^[135] successfully investigated soft hydrogel and hard UV curable acrylate urethanes to fabricate an artificial tendon-muscle-tendon system with spatially linear varying colors. The development of modern equipment and technologies has also made it possible to produce a material with non-linear gradients. Ren et al.^[92] developed a 3D printer equipped with a three-axis motion gantry, an active mixing device and a digital material feeding device (Figure 10c). During the printing process, mathematical functions were used to depict the graded distribution of material properties. Then, through gray-scale representation and controlling code generation, nano-sized Al_2O_3 particles were digitally fed into the printer to fabricate 1D, 2D, and 3D graded objects accordingly (Figure 10d).

Material extrusion-based FGAM is especially suitable for bio-printing since the multi-nozzle process allows to fabricate dual gradients (multi-materials and porous structures). However, its relatively low printing accuracy is unfavorable to achieve fine gradients. Besides, the inevitable post-processing (such as sintering) may cause severe shrinkage of the final component.

3.2.5. Materials Jetting

Material jetting, also categorized as PolyJet, utilizes UV light to cure and smooth parts made by depositing a liquid photopolymer. This state-of-the-art tool can utilize several inject heads to deposit multiple materials at one time and fabricate FGMs with various graded properties such as color, transparency, and stiffness.^[56] A digital material is a multi-material created by mixing different ratios of PolyJet photopolymers at specific concentrations before UV-light exposure, which greatly enlarges the range of printable materials available for PolyJet methods.^[91] Salcedo et al.^[91] used Tango Black+ (TB+, rubber-based material) and Vero White (VW+, ABS-based material) to fabricate circular and rectangular graded regions. The strain patterns according to FEA basically matched those obtained from the experimental tensile test, with only minor differences. Doubrovski et al.^[56] translated material properties into local material compositions using bitmaps to fabricate a prosthetic socket with the desired graded stiffness. Despite commercial software like Grab CAD is available for PolyJet to realize some basic physical property variations (e.g., graded color, transparency, and stiffness), limited materials can be used in the PolyJet FGAM process and the used materials are quite costly. The material's database needs to be enlarged to better satisfy the fabrication needs of FGM parts.

3.2.6. Vat Photopolymerization

Vat photopolymerization (including SLA, digital light processing, scanning, spinning, selectively photocuring, and continuous liquid interface production) fabricates objects by solidification of a liquid photosensitive resin using UV light. Although few examples are reported using vat photopolymerization, some emerging high-speed and high-precision fabrication technologies have been described, which are of interest and which may lead to future trends in FGMs. Martin et al.^[142] improved SLA devices by using a multicolor system to fabricate objects at high speeds (2 m h^{-1}) and with smooth surfaces through the realization of simultaneous photopolymerization and photoinhibition. In this approach, two illumination sources of different wavelengths (365 and 458 nm) are used to control the volumetric patterning by generating active polymerization of resin at one wavelength while confining its reaction at the other. A unique aspect of this system is the simultaneous initiation and inhibition of the photopolymerizable resin, which promises precisely manufactured FGSSs and FGMs. Brett et al.^[143] developed a new method, computed axial lithography (CAL), which can fabricate arbitrary geometries by volumetric solidification of a photosensitive resin. Different from conventional SLA devices, which add material layer-by-layer, CAL uses a video projector with a consistent rotation rate to output 2D

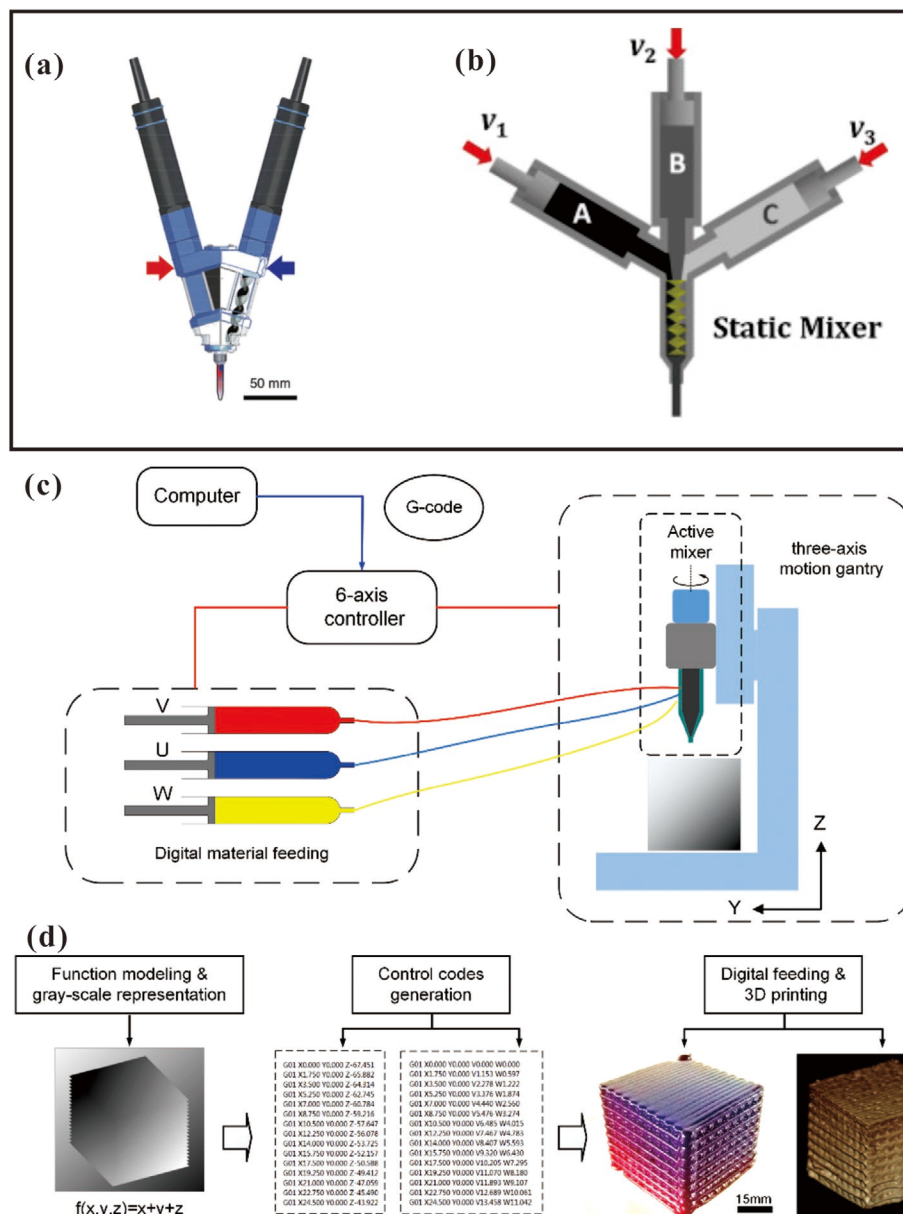


Figure 10. Schematic of a) a dual-extruder material extrusion device. Reproduced with permission.^[93] Copyright 2018, Wiley-VCH. b) A triple-extruder material extrusion device. Reproduced with permission.^[134] Copyright 2012, Elsevier. Gradient 3D printing system. c) Schematics of a gradient 3D printing mechanical setup and printing control system. d) Process of gradient 3D printing. Reproduced with permission.^[92] Copyright 2018, Elsevier.

images from all different angles to fabricate 3D objects in a photosensitive resin. This method allows for shaping parts in different locations and angles with great potential to enhance graded functionality.

3.2.7. Challenges for Current FGAM Technologies

Although the various FGAM methods have been exploited to manufacture FGMs, most of them are still far removed from being introduced in real industrial applications. Not only because of a lack of accurate representations of FGM designs but also because of non-optimized processing parameters

and lack of precision and stability of 3D printers when delivering graded raw materials. For example, Li et al.^[144] found a significant deviation in composition between the original pre-mixed powder fed to a printer and the final deposited material. As shown in **Figure 11a**, due to the difference in densities and sizes, dissimilar particles may move differently under the same gas flow, causing inconsistent material compositions. Thus, high precision in situ and real-time process monitoring methodologies are required for material characterization of FGAM processes. These techniques can help engineers better understand how microstructures and properties are affected during AM process, which is crucial for obtaining high-quality components. In the next section we will briefly introduce some

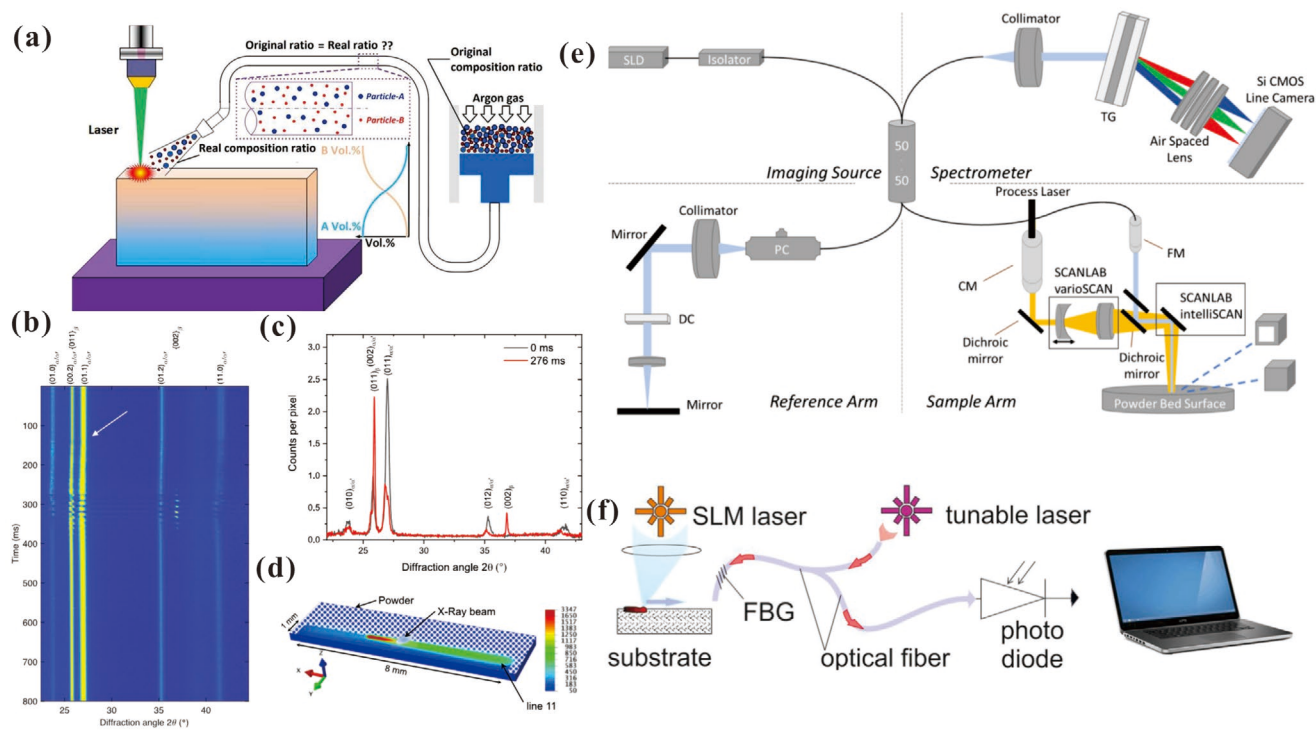


Figure 11. a) Fabrication of a customized material by laser melting deposition. Reproduced with permission.^[144] Copyright 2018, Elsevier. b) Phase evolution during printing of a single layer, shown as an intensity versus diffraction angle and time by stacking 16 000 individual diffraction patterns. The white arrow indicates the start of the printing process. c) Diffraction patterns recorded prior to printing and during printing of the 11th line at $t = 276$ ms. d) Schematic representation of the relative position of the laser, X-ray beam, and HAZ at $t = 276$ ms (temperature scale in °C). Reproduced with permission.^[145] Copyright 2020, Elsevier. e) Schematic illustration of commercial machines that integrate SD-OCT to the system. Reproduced with permission.^[18] Copyright 2018, Elsevier. f) Scheme of the fiber Bragg grating read-out system. Reproduced with permission.^[148] Copyright 2018, Elsevier.

potential in situ and real-time process monitoring techniques for AM. At the same time these may also lead to improved non-destructive testing and qualification methods for FGAM.

During the laser-based AM fabrication process, the deposited material undergoes rapid heating and cooling ($\Delta T \approx 10^3\text{--}10^5$ K s^{-1}). This abrupt change in temperature may suppress phase transformations and induce supersaturated phases, hot cracking, as well as thermal residual stresses.^[17] Hocine et al.^[145] used operando synchrotron X-ray diffraction to study phase transformations in Ti-6Al-4 V alloys during SLM printing with high temporal resolution (Figure 11b–d). During the laser-based AM fabrication of Fe-Fe₃Ni FGMs, the transformation of bcc- α -Fe phase into fcc-Fe₃Ni structures would lead to a different thermal expansion coefficient, inducing hot cracking and structural failures. Shen et al.^[146] fabricated an Fe-Fe₃Ni FGM using WAAM method and in situ characterized real-time phase transformations using the neutron diffraction instrument WOMBAT.

IR monitoring has been widely used to characterize melt pool geometry and temperature. Recently, Bartlett et al.^[147] adopted full-field IR thermography to in situ measure physical defects in AlSi10Mg specimen manufactured by SLM, with 82% lack of fusion defects successfully detected. High speed camera measurements such as optical image monitoring has also been implemented to detect defects. Large area spectral-domain optical coherence tomography (SD-OCT) was incorporated into a PBF system by DePond et al.^[18] for real-time monitoring of surface

roughness (Figure 11e). AE is another technique for monitoring AM product quality by precisely localizing defects and defect types and concentrations. In comparison with other methods, including imaging (using 2D data) or tomography (using 3D data), AE (using 1D data) is much faster and uses cheaper hardware. Shevchik et al.^[148] recorded AE signals using a fiber Bragg grating sensor to in situ monitor product quality during a SLM process (Figure 11f). Defects in stainless steel were detected in real-time using machine learning approaches and a detection reliability >85% was demonstrated in initial tests.

Next to challenges for researchers, there are also lots of challenges in FGAM for printer manufacturers as well as materials suppliers and end-users, varying from starting multi-material systems to application demonstrations. The field needs a long-term and continuous effort to develop a large portfolio of multi-material specifically designed for FGAM, as well as identifying manufacturing issues, and optimizing printing parameters for productivity and final part performance, which include: i) creation of database for multi-material systems; ii) upgrading of AM equipment (e.g., multiple lasers, thermal management, etc.); iii) in situ real-time monitoring of the 3D printing process, product inspection and quality management, which involve using high-speed camera imaging technology and the use of laser-induced breakdown spectroscopy (LIBS) and micro-CT scanning technology for 3D stereo processing of component measurements and high-precision inspection, and the use of machine learning and big data analysis methods to focus

on the manufacturing process, finished product composition, accuracy and defects, forming all a closed loop control system. Together with the establishment of an inspection and quality control system, it will ensure improved product reproducibility and reduce cost and loss of production; and finally vi) demonstrators that show the potential for large-scale industrial application. The whole loop system should consider materials, machines, builds, parts, tests, post-processes, design, CAE models, environments, as well as consider how to merge, trace and analyze complete FGAM data sets via fully configured portals, how to capture the full manufacturing process and ensure consistency and provide quality indicators, how to compare virtual FGAM to physical data, and how to improve print quality by correlating simulated to as-manufactured components. Furthermore, it should provide FGAM and non-FGAM data sets for process benchmarking and comparison.

4. Multifunctional Properties and Applications

Although there are still many challenges in FGAM with respect to design concepts, design shapes, printing accuracy, and types of materials, it has been widely studied in fields such as aerospace engineering, biomedicine, thermal management, electromagnetic shielding and optoelectronics. This section aims to provide an overview of the most promising potential applications, albeit continuous efforts are still needed to achieve potential industrial applications.

4.1. Mechanical Properties and Applications

The abrupt change in mechanical behavior at the interfaces between dissimilar materials in monolithic composites can easily lead to weak interfaces and/or mechanical failure. Compared with monolithic composites, FGMs can be much more robust because their gradient interfaces can help minimize thermal-mechanical stress concentrations, hence preventing delaminations at crack-sensitive regions and improving the durability of loadbearing structures. In recent years, polymer/ceramic/metal-based FGMs made by AM have been widely studied to overcome the shortcomings (such as crack initiation and propagation) of each of the individual components (Table 2). Ren et al.^[92] fabricated a polyurethane (PU) plate that possessed linear and parabolical variations in hardness as well as elastic modulus along its longitudinal direction (Figure 12a–d). These linear gradients in hardness and modulus were also observed in cantilever beam bending test (Figure 12e,f). By monitoring and simulating the forces acting on a topology optimized quadcopter's arm, Li et al.^[45] designed a lightweight functional graded cellular structured quadcopter's arm without compromising its performance compared to a traditionally designed structure (Figure 12g–j). Both simulation and experimental data showed that the optimized FGSs could significantly improve the structural stiffness of a quadcopter's arm. Similarly, many tools like cutting picks^[149] and wrenches^[47] have been fabricated with FGSs, improving and optimizing their mechanical behavior, demonstrating the feasibility of gradient cellular structures for lightweighting without sacrificing load-bearing

capabilities. Graded gyroid cellular structures (GCS, a kind of functionally graded cellular structure) with the gradient parallel to the loading direction exhibited layer by-layer deformation and failure behavior. Mathematical models were developed to predict and customize the mechanical properties of GCS by optimizing the relative density of each layer (Figure 12k,l).^[150] A 3D gel-printed TiC-high manganese steel cermet showed gradient distributions in density, hardness, transverse failure strength, abrasion wear resistance and impact toughness due to its graded structure.^[149]

4.2. Biocompatibility and Biomedical Applications

The most common effects of biological gradients are their mechanical functions, for examples, load bearing and support (e.g., bones or plant stems), resisting contact and impact damage (e.g., shark teeth,^[163,164] spider fangs,^[165,166] fish scales^[167,168]) and interfacial strengthening and toughening (e.g., tissues or organs), offering a variety of functional properties, including light collection and transmission, sensing and actuation in response to environmental stimuli, and control of liquid flow.^[169,170] Biological FGMs demonstrate a rather complex structural diversity and hierarchy.^[170,171] The generation of structural characteristics basically involves the local arrangement of i) constituents (e.g., the loose and dense aragonite units in shells^[172]); ii) distribution (e.g., cellular, fibrous, tubular, etc.); iii) dimensions (e.g., multiple length-scales down to the nanometer level); iv) orientations of structural building units (e.g., successive arrangements of layers with different orientations of constituents);^[173] v) gradient interfaces (e.g., junctions); or vi) integration of multiple gradients (e.g., parallel combinations and hierarchical gradients), as shown in Figure 13a–h.^[22]

FGAM has great potential to fabricate tissue engineered and biomedical devices with complex bioinspired gradients, such as scaffolds, bone implants, artificial muscles and human organs.^[133,178–181] For example, Martin et al.^[177] set up an SLA-based AM system, termed as 3D magnetic printing, to finely control the direction of ceramic microparticles at voxel level using a magnetic field. The developed ceramic/polymer composites with complex bioinspired reinforcement architectures (Halioitidae sp. abalone shell, dactyl club of the peacock mantis shrimp and the mammalian cortical bone, Figure 13i–k) showed improved mechanical properties (stiffness, strength, and hardness) compared with single-phase materials. Next, we will introduce some cases that used FGAM to create bioinspired gradients.

Compared with traditional uniform porous materials, FGSs show graded mechanical properties (e.g., lightweight, high specific strength and stiffness) and provide a gradient pore distribution and size, yielding the potential to tailor pore space for tissue growth. Continuous functionally graded porous titanium scaffolds were manufactured by SLM with a tailored elastic modulus (0.3–0.6 GPa) and yield stress (3.8–178 MPa) by adjusting the graded volume fraction, resulting in properties comparable to those of cancellous bone.^[179] Cell locality gradually changed through the entire material volume and was related to variations in structural characteristics, chemical compositions, or constituents.^[65] Costantini et al.^[182]

Table 2. Mechanical properties and features of FGM made with various materials and printing methods.

FGM types	Printing method	Composition	Properties and features	Refs.
Metal-based	DED	Cr-Ni	Microhardness from substrate (159.7 HV) to top surface (545.4 HV)	[151]
		Ti-6Al-4 V to 304L stainless steel (SS304L)	Microhardness from 200 to 850 HV	[152]
		304L stainless steel incrementally graded to Inconel 625	Microhardness from 190 to 240 HV	[68]
		304L to Invar 36 gradient alloy	Vickers hardness from 60 to 125 HV and elastic modulus ranging from 160 to 240 GPa	[67]
		Functionally graded Ti6Al4V/TiC	Vickers hardness from 300 to 1200 HV with the highest hardness four times that of the substrate (Ti6Al4V)	[153]
		Ti-6Al-4 V to 304L stainless steel	Vickers hardness from 300 to 500 HV and elastic modulus ranging from 100 GPa to 150 GPa	[154]
		Ti-6Al-4 V to Invar 36	Vickers hardness from 150 to 800 HV	[67]
		Ti-6Al-4 V to SS316	Vickers hardness from 270 to 400 HV	[155]
		Graded Ti/Ti6Al4V	Hardness from 1.8 GPa to 3 GPa and elastic modulus ranging from 105 GPa to 130 GPa	[156]
		Ferritic and austenitic alloys	Vickers hardness from 125 to 350 HV	[80]
		Addition of alloying elements (Nb and Zr) in 35Nb-15Zr	Hardness from 280 to 360 HV and elastic modulus ranging from 70 GPa to 115 GPa	[157]
		Metal-based	PBF	Al and Al + Al ₂ O ₃ , Ti6Al4V
IN718	Longitudinal samples showed lower tensile strength (UTS = 1101 MPa, $\sigma_{0.2}$ = 710 MPa) but higher elongation (ϵ_f = 24.5%) than transverse samples (UTS = 1167 MPa, $\sigma_{0.2}$ = 850 MPa, ϵ_f = 21.5%)			[158]
Iron FGM with four structures: a uniform structure with a 0.2 mm strut thickness (S0.2); FGS with a strut thickness changing from 0.2 mm at the periphery to 0.4 mm in the center (Dense-in); FGS with strut thickness starting from 0.4 mm at the periphery and decreasing to 0.2 mm in the center (Dense-out); and a uniform porous structure with a strut thickness of 0.4 mm (S0.4)	S0.2 group: highest yield strength of 10.7 MPa and elastic modulus of 892 MPa S0.4 group: highest yield strength of 53.1 MPa and elastic modulus of 2816 MPa Dense-in group: highest yield strength of 32.9 MPa and elastic modulus of 1767 MPa Dense-out group: highest yield strength of 30.5 MPa and elastic modulus of 1754 MPa			[159]
Polymer-based	Material extrusion	Nano-Al ₂ O ₃ , photosensitive resin	Different materials color, nano-Al ₂ O ₃ concentration, and mechanical properties (a range of hardness from 900 Pa to 54 000 Pa)	[160]
		Acrylates-methacrylates	Wide range of stiffnesses and strengths, and strain at break ranging from 67% to 753%	[93]
	Vat photopolymerization	A white resin of FLGPWH04 version (ρ_{sol} is 1.3 g ml ⁻¹ , E_{sol} after curing process is 2.8 GPa, Formlabs company) General commercial photosensitive resin	The compressive stress of graded Schwarz P structure ranging from 0 to 16 MPa, the five layers of the graded structure being identified from the stress peaks Elastic modulus, yield stress and critical buckling stress sharply rose in upper layers (total 9 layers, varying by 5% in each layer) while the Poisson's ratio is nearly constant in all layers	[161] [162]
Ceramic-based	LOM	TiC-20 wt%Ni	Three-point bending strength was 950 MPa. The average density of TiC-Ni FGM was larger than 5.2 g cm ⁻³ .	[163]
	DED	SiC particles reinforced Ti6Al4V alloy composite FGM layers	Maximum shear strength of a ZrC-SiC ceramic and Ti6Al4V alloy coated with FGM layers was 91 MPa	[164]
		Hydroxyapatite, polymeric additives V5.2 and V12 (10 and 14 wt%)	Internal channels ranged between 450 and 570 μ m, the mechanical strength of dense test parts was up to 22 MPa	[165]

employed a valve-based flow-focusing junction (vFF) in which the size of the orifice could be adjusted in real-time to generate foams with an in-line controlled bubble size. Here the vFF was mounted on top of an extrusion printer to fabricate a long bone tissue engineering model with layered and smoothly graded porous structures and pore sizes varying from 80 to 800 μ m. Biodegradability is crucial both for full tissue regeneration and for the prevention of implant-associated infections

in the long term. Li et al.^[157] reported a topological design with functional gradients that controlled the fluid flow, mass transport, and biodegradation of AM-fabricated porous iron specimens with up to fourfold variation in permeability and up to threefold variation in biodegradation rate. Han et al.^[183] used SLM technology to prepare titanium/hydroxyapatite (Ti/HA) with quasi-continuous ratios, in which the ratio of HA varied from 0 to 5 wt% in each functional gradient, providing a wide

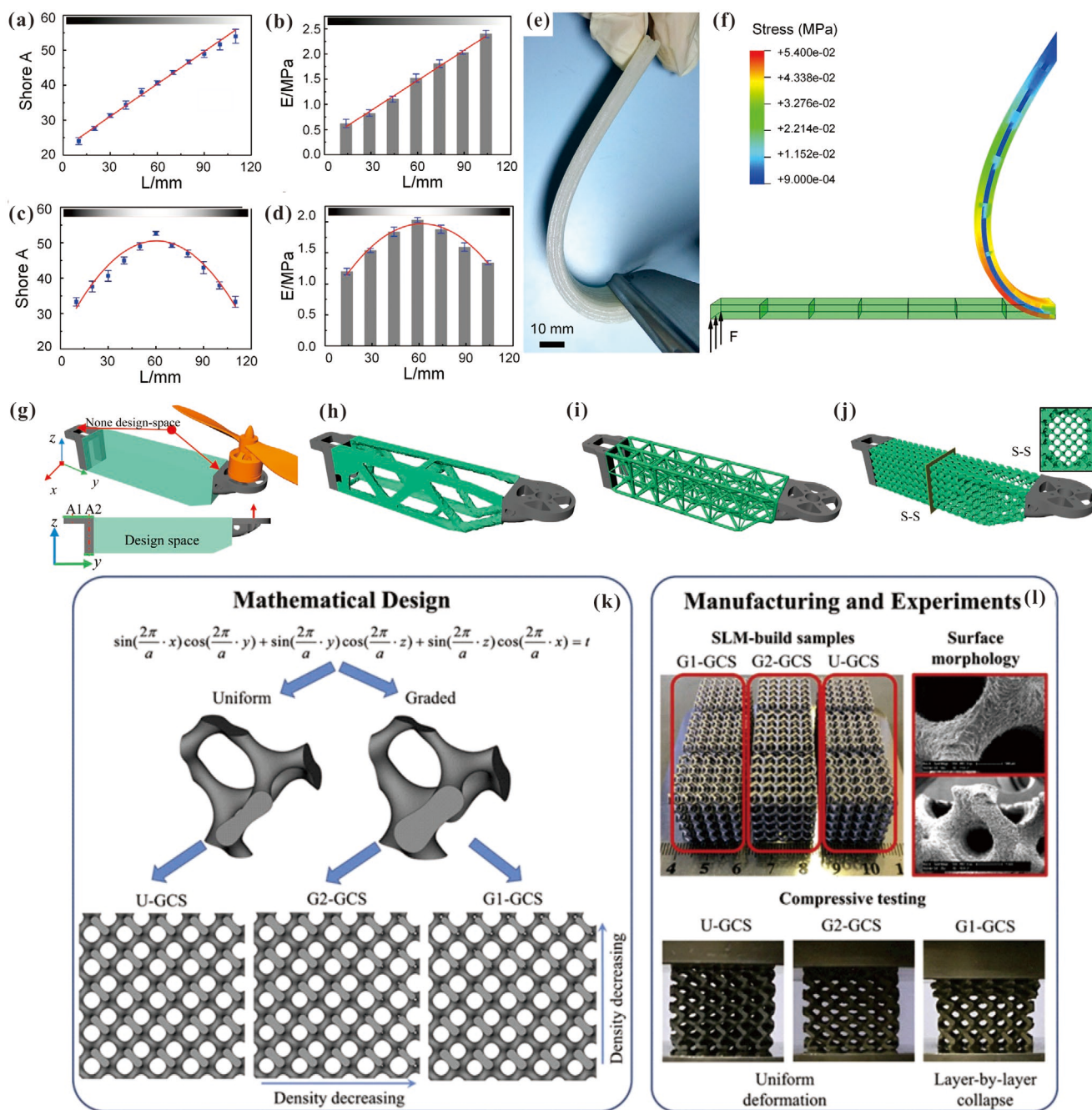


Figure 12. Mechanical properties of printed long PU plates. a) Hardness and b) modulus of PU plates with linearly distributed components along their lengths as a function of position. c) Hardness and d) modulus of PU plates with parabolic distributions as a function of position. e) Cantilever bending test of the printed object with linear gradient modulus and f) finite element simulation of the model with linear gradient modulus. Reproduced with permission.^[92] Copyright 2018, Elsevier. Quadcopter's arm optimization results: g) initial shape of the arm; h) standard topology optimization result; i) traditional truss design result; j) functionally graded cellular structure-based optimization result. g–j) Reproduced with permission.^[45] Copyright 2018, Elsevier. k) Modeling of graded gyroid cellular structures (GCS); l) SLM-fabricated GCS, surface morphology of SLM-fabricated GCS, and compressive test of GCS. k, l) Reproduced with permission.^[150] Copyright 2019, Elsevier.

range of nanohardness (5.11–8.36 GPa) and fracture toughness (3.41–0.88 MPa m^{1/2}), which could be tailored to match those of cortical and cancellous bones. Kawai et al.^[184] designed and 3D printed a functionally graded scaffold made of polycaprolactone (PCL) and β -tricalcium phosphate with spatially controlled porosity, degradation and mechanical strength to reconstruct

necrotic bone tissue in the femoral head. It was shown that a combination of FGS scaffolds and bone marrow-derived mononuclear cells can improve the core decompression outcome in the early stage of osteonecrosis of the femoral head by providing both enhanced biological and biomechanical cues in the osteonecrotic area.^[185] Klein et al.^[186] used a bio-printing process

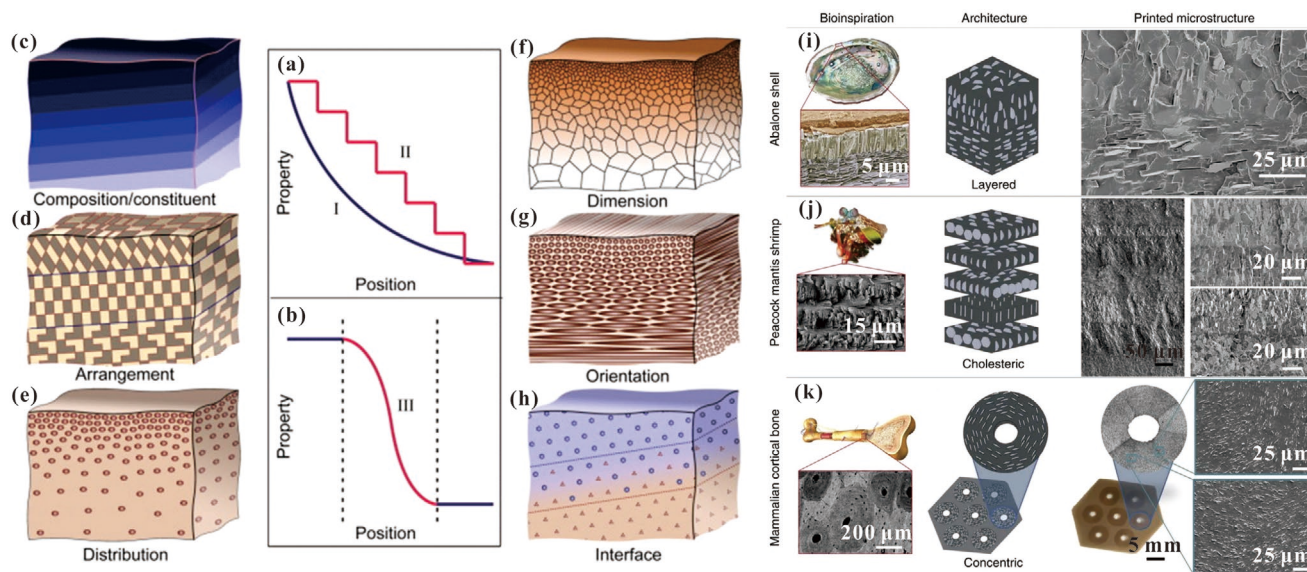


Figure 13. Local property profiles and basic forms of gradients in biological materials. a) Local properties change either gradually (I) or in a stepwise manner (II) through the entire material volume. b) Local properties vary continuously across the interface between dissimilar components. c–h) Gradients in biological materials are fundamentally associated with changes in chemical composition and constituents, and c) structural characteristics, including the arrangement (d), distribution (e), dimensions (f), and orientations (g) of building units. h) Gradient interfaces in biological materials. Reproduced with permission.^[22] Copyright 2017, Elsevier. Original structures, simplified and 3D magnetic printed structures of i) *Haliotidae* sp. abalone shell. Reproduced with permission.^[174] Copyright 2013, AAAS. j) Dactyl club of the peacock mantis shrimp. Reproduced with permission.^[175] Copyright 2014, Elsevier. k) The mammalian cortical bone. Reproduced with permission.^[176] Copyright 2006, Elsevier. i–k) Reproduced with permission.^[177] Copyright 2015, Springer Nature.

to print layers containing cells from different zones of articular cartilage. Distinctly different responses of human chondrocytes on the graded hydrogel materials were observed, allowing for cell function control and spatial distributions of cells or signals (Figure 14a,b). Another example of an FGAM implant was a novel porous titanium craniofacial part that had a graded porosity and density ideal for patient-specific implants. These maxillofacial and craniofacial implants demonstrated great compatibility, matched functional performance characteristics, and reduced weight (Figure 14c,d).^[86]

As for more complicated organs, it is particularly critical for implant materials to minimize interfacial stress and wear. However, homogeneous materials like hydrogels are usually unable to meet the performance requirements of biological tissues.^[22] Mechanical gradients inspired by biological materials can alleviate local mechanical stresses and help to overcome certain constraints in traditional engineering systems. Some cases have fabricated graded multicomponent hydrogels and other biological materials^[22,133,178,186–188] as well as designed biomimetic and tissue engineering scaffolds with tailored pore sizes, porosity, and scaffold-tissue interconnectivity (Figure 14e).^[189–191] Bakarich et al.^[133] fabricated an artificial meniscus using fiber reinforced hydrogels with directionally distributed hardness and stiffness through an extrusion-based printing process. A bio-inspired artificial tendon was also developed, which consisted of connective tissue with graded mechanical properties between muscle and bone (Figure 14f,g). In addition, similar research was also applied to a meniscus cartilage.^[178] Likewise, Kokkinis et al.^[91] printed a graded human intervertebral disc with a soft core and hard surface. The connection parts

displayed a descending gradient, and exhibited great defect tolerant mechanical properties and tunable failure behavior (Figure 14h).

Graded biomaterials are important in organic systems and can provide biological and structural functions (Table 3). Previously, biomimetic systems used homogeneous materials for shape driven designs, which encountered great challenges to mimic the heterogeneous properties and microstructures of biological tissues.^[91] FGAM allows composite biomedical implant materials with gradient properties to be manufactured directly. However, bio-printing technologies must overcome several issues, such as microvascularization and bioink longevity, before attempting to print a full organ. Some preliminary results can be seen in literature, FGAM implants are far from real clinical application. It is believed that further development of FGAM holds great potential for manufacturing multi-material tissue engineering scaffolds with consideration of various types of cells, cell growth, cell adhesion and migration factors.

4.3. Thermal Properties and Thermal Management

The uniquely graded distribution of FGMs alleviates thermal stress concentrations and hence prevents delaminations at crack-sensitive regions. Therefore, FGMs were exploited to improve the durability of heat exchangers. Onuike et al.^[202] fabricated bimetallic materials comprising Inconel 718-Copper alloy via SLM and reported that these bimetallic materials, tailored with graded thermal properties, exhibited 250% and 300% increases in thermal diffusivity and conductivity, respectively,

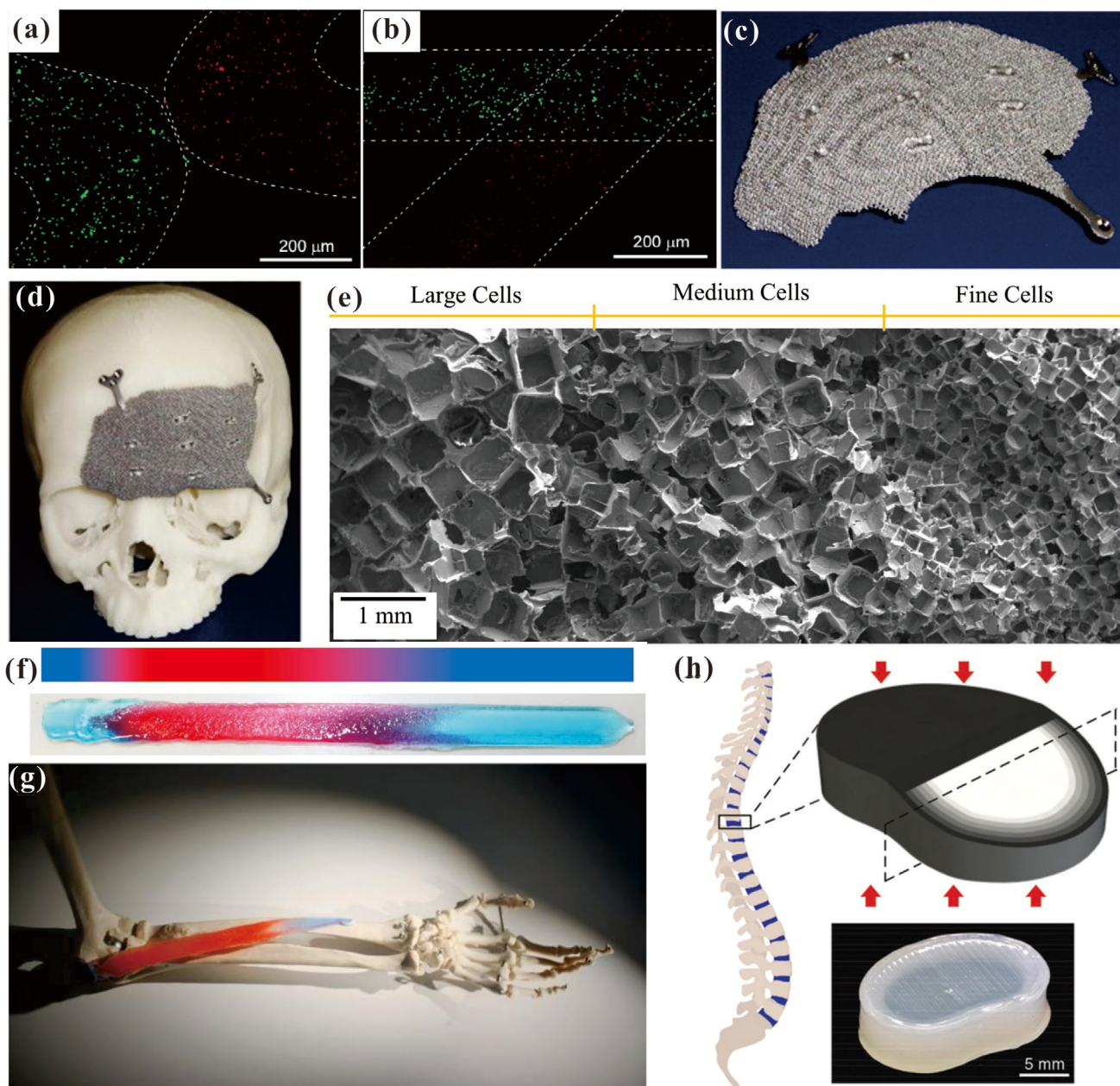


Figure 14. Printed cells labeled with fluorescent cell tracking dyes (red and green) maintain distinct localization in a) adjacent and b) layered printed alginate fibers. Reproduced with permission.^[190] Copyright 2009, Wiley-VCH. c) Porous Ti alloy implant fabricated by EBM. d) Titanium alloy implant fitted to a skull model. Demonstrations of gradient printing inspired by the human tendon–muscle–tendon system. Reproduced with permission.^[88] Copyright 2011, Elsevier e) SEM micrographs of functionally graded PLA open-cell foam suitable for different cell cultures. Reproduced with permission.^[192] Copyright 2014, Springer Nature. f) Model representing gradients as the transition from blue to red and a graded structure of tendon–muscle–tendon system printed with bio-gels. g) Arm showing muscle attached to skeleton by a tendon. Reproduced with permission.^[135] Copyright 2017, Elsevier. h) Illustration of the loading condition and the gradient design of an artificial intervertebral disc. Reproduced with permission.^[93] Copyright 2018, Wiley-VCH.

compared with neat Inconel (Figure 15a). Meanwhile, Hofmann et al.^[71] fabricated a graded alloy (Figure 15b,c) via SLM and reported significant effects on coefficient of thermal expansion (Figure 15c, solid red lines). Graded thermal properties occurred at a distance from 15 to 25 mm across the alloy, which was desirable for gradually transferring heat in the heterogeneous alloy.

Graded ferritic and austenitic alloys offer a solution for creating dissimilar metal joints with spatial variations in chemical compositions and microstructures. Functionally graded-alloy joints can retard carbon transport more effectively and therefore reduce carbon accumulation in austenite of nuclear power plants.^[80] In addition, 3D printed graded densities of the same metal can also contribute to minimize abrupt changes, residual

Table 3. Mechanical properties and porosities of AM fabricated FGM and FGS architectures for biomedical applications.

	Material	Porosity [vol%]	AM method	Mechanical properties	Applications	Refs.
FGM	Alginate/poly(acrylamide)	—	Material Extrusion	Smooth and continuous gradient of modulus 0.5–3.0 MPa	Bio-inspired structures such as artificial tendons	[135]
	Alginate/acrylamide gel precursor solution and an epoxy-based UV-curable adhesive (E_{\max} 904 Gel-SC) and fibers	—		Physical characteristics ranging from soft and wet to hard and dry	Artificial meniscus cartilage; robotics (artificial muscles), and bionics (tissue scaffolds and artificial organs)	[181]
	Soft elastomeric to hard brittle polymer to functionally graded ceramic composite	—	SLA	Designed composite lightweight metamaterials with tailored stiffness and toughness	Flexible armor, artificial muscles, actuators, and bio-mimetic materials	[193]
	Ti/HA	—	SLM	Hardness (5.1–8.4 GPa) Vickers hardness (3.4–5.7 GPa)	Orthopedic applications	[186]
FGS	Ti-6Al-4V	54–60	SLM	Elastic modulus (3.4–26.3 GPa) Linear relationship of compressive strain, strength and modulus	Bone scaffolds	[194]
	CoCrMo	Pore size 30– 50 μm		48% lighter and 60% more flexible than a traditional fully dense stem	Orthopedic implants	[195]
	Ti6Al4V	49.7–70.3		Effective stiffness (0.6–2.9 GPa) and compressive strength (7.3–163.0 MPa)	Porous titanium cranioplasty plate	[88]
	CoCrMo	≥ 50		12% (Gruen zone 7) and 36% (Gruen zone 6) increase in the von Mises stress in the proximal-medial femur	Implanted femur	[196]
	Ti-6Al-4V	50–100		Comparable elastic modulus (3.8 GPa) with natural cortical bone	Implant scaffolds	[156]
	Ti-6Al-4V	29.9–78.6		Reduced effective modulus of implants by 75–80%	Bone scaffolds and orthopedic implants	[197]
	Ti-6Al-4V	38–75		Elastic modulus (3.7–5.7 GPa) and yield stress (27.1–84.7 MPa) situated between those of cancellous bone and cortical bone; Heat treatment reduced the strength by 13–56%	Bone tissue engineering	[198]
	Ti	Graded volume fraction from 8% to 20%		Elastic modulus (0.3–0.6 GPa) and yield stress (3.8–17.8 MPa) comparable to those of cancellous bone.	Bone implant	[182]
	Ti-6Al-4V	37.9–79.2		Compared to 117.2 GPa for conventional wrought Ti-6Al-4 V alloy used for implant production, 30.5 GPa similar to human bones.	Orthopedic implant	[199]
	Ti-6Al-4V	21.0–91.3		Combination of low density (1.9 g cm^{-3}), moderate Young's modulus (10.4 GPa), high yield stress (170.6 MPa), high maximum stress (201 MPa) and favorable ductility,	Orthopedic implants and bone substitutes	[200]
	Ti-6Al-4V	75–85	EBM	Higher porosity and mismatch at interfaces; the degree of mismatch (or degree of strut overlapping) plays a more dominant role	Biomedical implant foams	[201]

stresses and distortions in dissimilar alloy joints,^[87] which can be exploited in aerospace, automotive, and marine industries.

With the development of launch and hypersonic vehicles, more complex geometries have been applied to the design of integrated thermal protection (ITP) structures.^[67] Inspired by the structure of the spruce stem (Figure 15d), Kaijie Lin et al.^[203] used SLM to fabricate a series of ITP structures with different graded hollow tubular sections (Figure 15e,f)

via SLM, resulting in the lowest bottom surface temperature of 263 °C (Figure 15g–l), which was 21 °C lower than that of other structures. Zhang et al.^[100] created a graded multi-metal heat exchanger with a designed graded structure, which displayed better thermodynamic properties (e.g., pressure drop, temperature distribution, and heat transfer coefficients, Figure 15m–o) and improved the heat distribution performance by about 20–30 $\text{W} \cdot \text{m}^{-2} \cdot \text{K}^{-1}$ compared to those

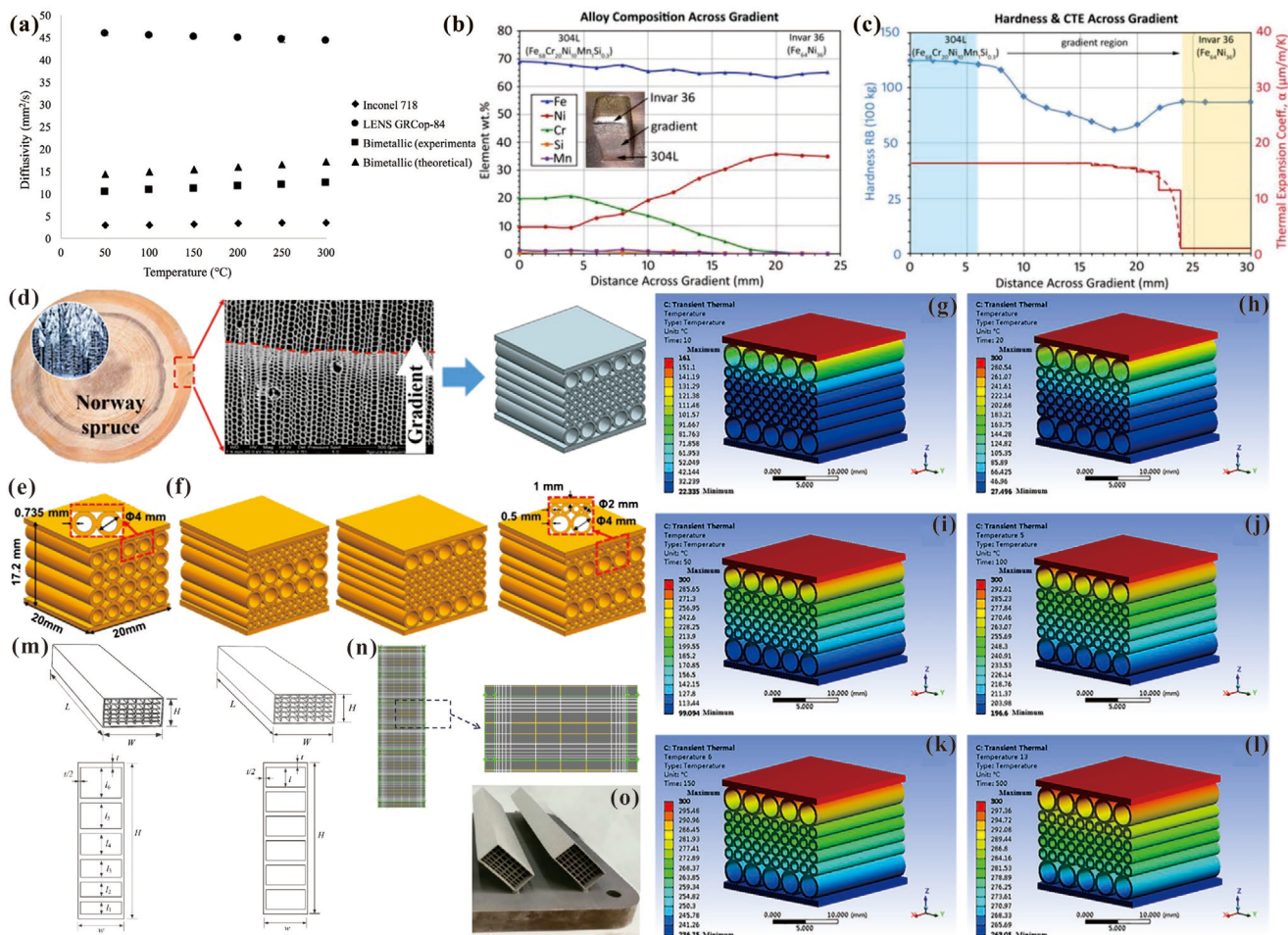


Figure 15. a) Thermal diffusivity as a function of temperature for a bimetallic structure of Inconel 718 and copper-based alloy GRCop-84, and pure Inconel 718 and GRCop-84. a) Reproduced with permission.^[202] Copyright 2018, Elsevier. b) Plot of composition versus distance for a 304 L to Invar 36 graded alloy post. c) Plot of Rockwell B hardness and coefficient of thermal expansion versus distance for the graded alloy from (b). Reproduced with permission.^[71] Copyright 2014, Springer Nature. d) Design inspiration of ITP structures. e) Non-graded structure. f) Three-graded structures. Transient temperature distribution of GB structure at different times: g) 10 s; h) 20 s; i) 50 s; j) 100 s; k) 150 s; l) 500 s. Reproduced with permission.^[203] Copyright 2019, Elsevier. m) Graded and non-graded honeycomb with varying cell size. n) Meshes of a CFD model for honeycomb structures. o) Samples fabricated by AM. Reproduced with permission.^[100] Copyright 2018, Elsevier.

of a conventional heat exchanger with a uniform honeycomb structure.

4.4. Energy Absorption Properties and Electromagnetic Interference Shielding

With the development of artificial intelligence technology, soft robotics need to be able to interact easily with humans; for instance, robots with graded mechanical properties can be designed to absorb impact energy.^[204] The graded stiffness of soft robotic shells could transfer the combustion power that drives the robot by transferring the physical damage and external energy into its own movement.^[204] Table 4 lists a summary of recent studies on FGM- or FGS-based energy absorption systems.

Density-graded lattices also have excellent energy absorption properties (Table 4), and meet the demands of various

applications such as personal protection equipment and packaging materials.^[140] By combining graded honeycomb structures and graded material densities, the plateau stress and specific energy absorption were higher than of homogeneous materials by up to 67% and 72%, respectively.^[140]

Radar absorbing structures (RAS) are employed in structural stealth technology applications. However, conventional RAS structures cannot match the impedance of the environment because of a low dielectric permittivity of their surface layer or the lack of propagating paths within their structures.^[205] A metamaterial with graded structures can have adjustable stiffness through changes in geometry while keeping a constant mass. Yin et al.^[206] created a gradient refraction RAS for application to stealth aircraft that was composed of three layers (gradient refractive index radar absorbing structure, GRINRAS, Figure 16a), and showed that the absorption capacity of GRINRAS was better than 10 dB at 12–18 GHz (Figure 16b).

Table 4. Summary of studies on FGM and/or FGS-based energy absorption.

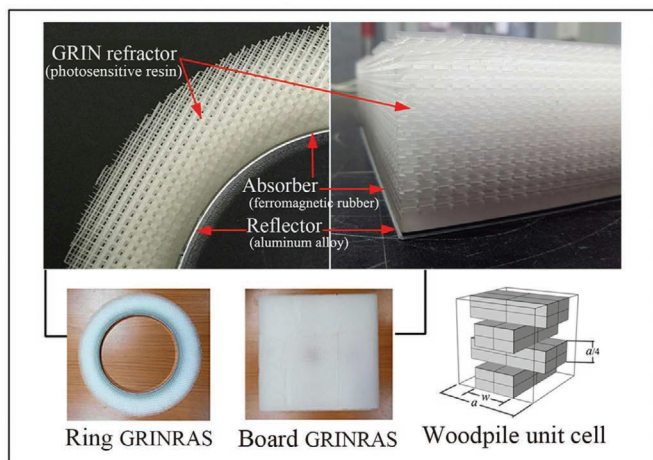
AM method	Composition	Types of energy	Compare data	Graded material/structure	Applications	Refs.
SLM	Ti-6Al-4V	Strain and stress	Plateau stress and specific energy absorption of the FGM were higher than for uniform structures by up to 67% and 72%, respectively.	Graded honeycomb structure	Packaging material, personal protection equipment and surgical implants	[140]
	Ti-6Al-4V	Strain and stress	Specific energy absorption (SEA): Uniform: 0.0172 MJ kg ⁻¹ Graded: 0.022 MJ kg ⁻¹ Collapse strength was increased by 25%.	Graded rhombic unit cell		[80]
	Al-12Si	Strain and stress	Energy absorption: Uniform: 2.6 Wv (MJ m ⁻³) Graded: 3.2 Wv (MJ m ⁻³)	Graded lattice structure		[207]
	Al-Si10-Mg	Strain and stress	Energy absorption: Uniform: 5.7 Wv (MJ m ⁻³) Graded: 6.3 Wv (MJ m ⁻³)			[139]
EBM	Pure copper	Strain and stress	Graded foams possessed 16–18% higher energy absorption capacity as compared to uniform foams.	Graded open cell ordered foams	Thermal mechanical monolithic heat exchanger devices	[208]
SLA	Ferromagnetic rubber	Electromagnetic waves	Absorption capacity of GRINRAS was better than –10 dB at 12–18 GHz.	Graded woodpile unit cell	Stealth aircraft	[206]
DIW	Polylactic acid	Electromagnetic waves	Widest absorption band: Single-layered composite: 4.4 GHz Graded multilayer: 4.5–40 GHz	Graded multilayer structure	Stealth aircraft	[209]

4.5. Photoelectric Properties and Optoelectronics Devices

Spatially varied refractive index gradients have been applied in anti-reflective surfaces, passive beamformers and graded index lenses.^[210–213] Conventional technologies, including ion exchange and sol–gel techniques, with common limitations such as long processing times (typically >100 h) and limited component sizes (typically <13 mm), can be overcome by using FGMs and FGSs.^[214] Roper et al.^[210] printed dielectric powders (ECCOSTOCK HiK) on fabric-glass

composite substrates (S-glass/cyanate ester fiber reinforced composites) via ultrasonic powder deposition. By printing and stacking multiple layers using single-layered dielectric powder (**Figure 17a,b**), a final composite with a graded variation of permittivity in the vertical direction was created.^[211] Through the 2D phase response near the surface of the lens at an incident frequency of 15 GHz, the measurement in the *x*-direction and *x*-*y* plane (**Figure 17c,d**) showed graded dielectrics, indicating that graded index lenses had been successfully produced.^[210,212,215]

(a) Gradient layered structure



(b) Electromagnetic property

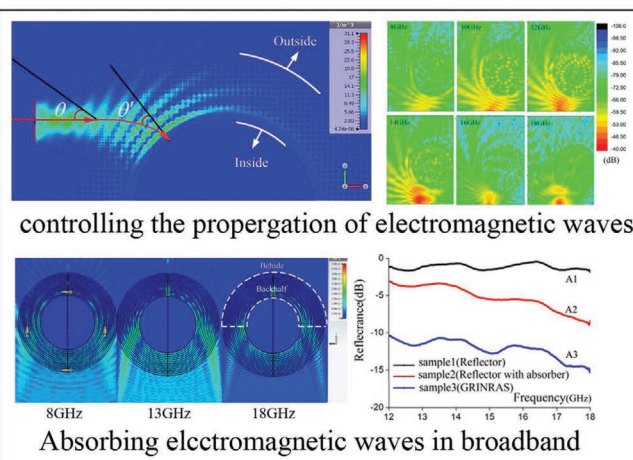


Figure 16. a) Photographs of fabricated GRINRAS: local and top view of a ring and board-shaped GRINRAS with a woodpile unit cell. b) Power density of the electromagnetic wave beam going through the ring GRINRAS at 8, 13, and 18 GHz; electromagnetic waves going in a direction deviating from the center of the ring GRINRAS by 60 mm, the reflectance of the three board samples at 8–18 GHz in the Ku band. Reproduced with permission.^[206] Copyright 2018, Elsevier.

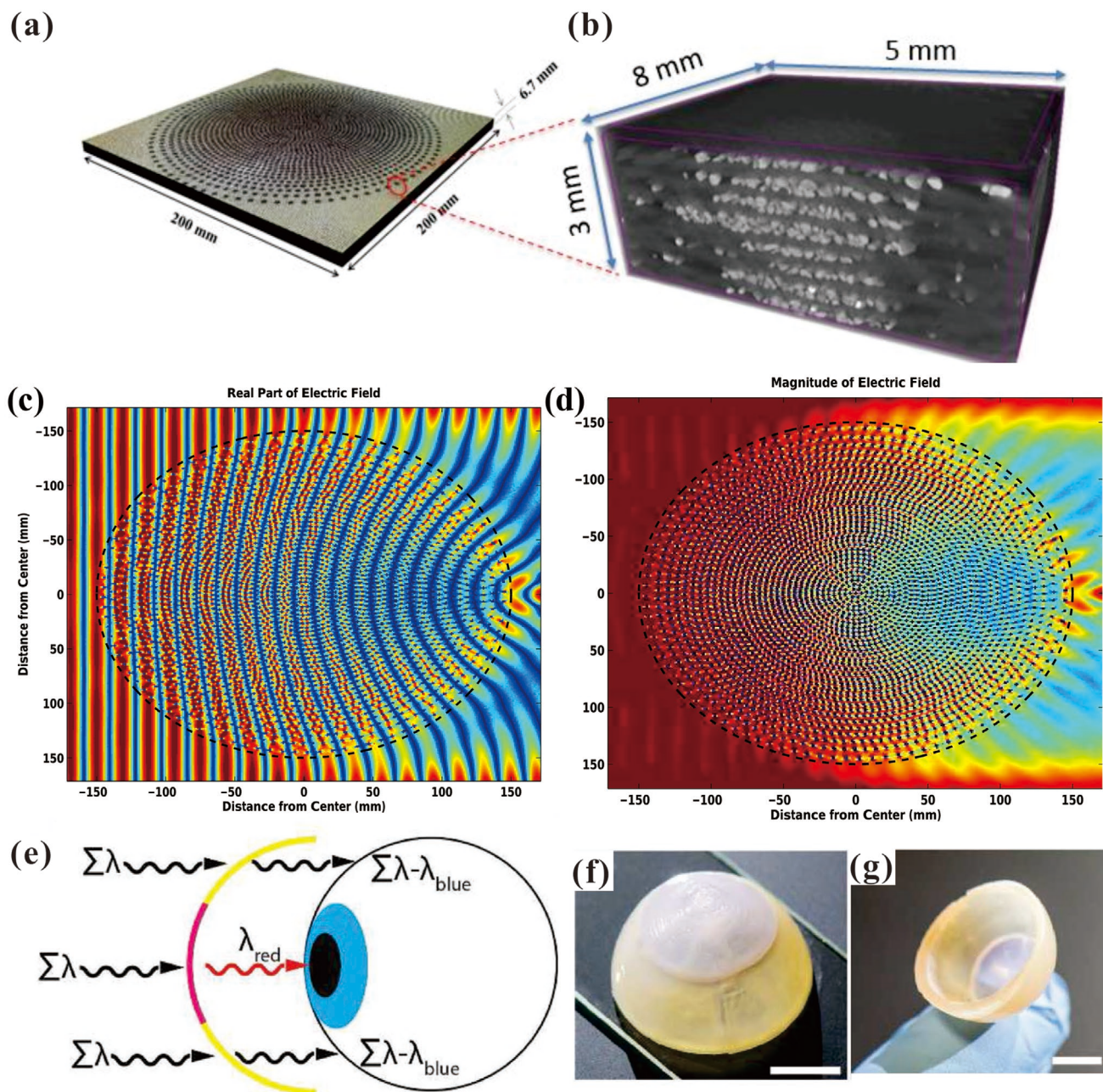


Figure 17. a) Printed sample; b) micro-computed tomography (micro-CT). Reproduced with permission.^[211] Copyright 2015, IEEE. c) Real part and d) magnitude of a plane wave incident on a water cylinder Luneburg lens. Reproduced with permission.^[215] Copyright 2016, IEEE. e) Concept of the gradient plasmonic night vision contact lens. Photographs of a 3D-printed plasmonic night-vision contact lens on f) glass slide and g) finger. Reproduced with permission.^[216] Copyright 2017, Wiley-VCH.

The functionally graded plasmonic devices, fabricated by Haring et al.^[216] through the selective expression of red and blue light via AM processes, have led to a novel functionally graded plasmonic night-vision contact lens (Figure 17e–g) that filters visible wavelengths other than red light (650 nm) from entering the pupil and prevents blue light (475 nm) from entering the surrounding regions of the eye. A solid insulator plays an important role in mechanical support and electrical insulation between the different electric potential conductors.^[217,218] Li et al.^[217] confirmed that an FGM insulator can

significantly improve the electric field distribution while the maximum electrical field strength (E_{max}) was greatly reduced. Through topological optimization, an optimized FGM insulator was obtained with a uniform electrical field inside/along the insulator surface. An FGM insulator was created by Li et al.^[218] via an FDM technique with the maximum value of the electrical field being significantly reduced by over 42%, resulting in an optimal electrical field distribution.

In addition to the optoelectronic materials, fabrication of graded magnetic bimetallic structures was also completed

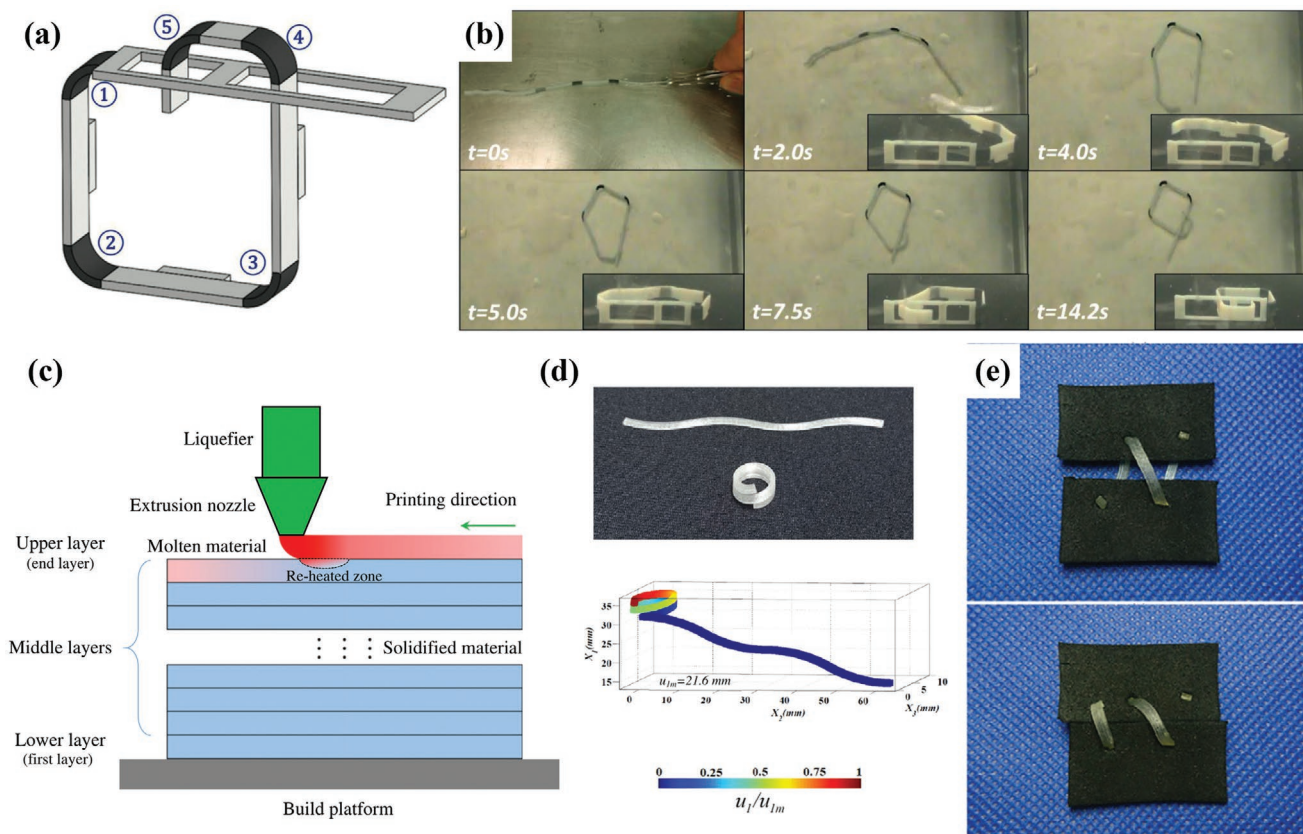


Figure 18. a) Schematic view of the interlocking gradient SMP. b) Shape-recovery process of SMP component. Reproduced with permission.^[226] Copyright 2015, Elsevier. c) How graded materials are printed by FDM. d) 4D-printed metamaterial with self-folding capability and simulation of the final configuration after heating and cooling. e) 4D-printed loose knot and shrinkage of a fiber by heating. Reproduced with permission.^[227] Copyright 2017, Elsevier.

using a laser shaping system.^[219] The graded magnetic material showed a transition from non-magnetic steel 316 (SS316) to magnetic steel 430 (SS430), and a smooth transition in microhardness value of 266 to 174 HV, while magnetic properties only existed at the SS430 side.^[219] Another combinatorial graded alloy with magnetic properties was produced via a laser-based AM method, exhibiting a saturation magnetization (M_s) value of 248 emu g^{-1} from 199.3 emu g^{-1} for Co100-xFex alloys, and a value of 168.7 emu g^{-1} from 119.8 emu g^{-1} for Ni100-xFex.^[220]

4.6. Other Applications

4.6.1. Shape Memory, 4D Printing, and Metamaterials

Another potential application of FGAM is in shape memory materials (SMM) which can respond to appropriate stimuli and undergo a geometrical transformation according to a predetermined sequence.^[57] Recently, number of studies have focused on 4D printing, which is a concept of producing SMM via 3D printing.^[220–222] With the tailoring of microstructural properties, 4D-printed components made via FGAM can realize more complicated geometrical transformations (such as functionally graded folding, graded curling, graded contracting, graded expansion and other transformations^[223]) by strategically

controlling the density and directionality of stimuli-responsive materials.^[57] Research into 4D printing of FGMs or FGSs have been reported recently.^[224,225] Yu et al.^[226] demonstrated functionally graded SMM made by 3D printing (Figure 18a), where the original shape was recovered by changing the compositions of materials to control the glass transition temperature (Figure 18b). AM technology may enable the manufacture of more advanced SMM with gradual variations in structures and compositions.

Bodaghi et al.^[227] showed that 3D printing technology can transform engineered metamaterials with performance driven functionalities, showing that FDM has the potential to fabricate 3D shape memory polymers (SMP, Figure 18c). It was shown that these 4D-printed metamaterials have great potential in mechanical or biomedical applications like structural and dynamical switches, deploying stents, self-coiling and self-conforming substrates, or self-tightening surgical sutures (Figure 18d,e).

By introducing zirconia components with graded microstructures, a brick-and-mortar like component consisting of graded dense (<1% porosity) and porous (5% porosity) regions can be made with a combination of properties. This opens the door to producing ceramic-based 4D components via AM, such as multi-material/color/functional components.^[228] FGAM produces seamless material integration and eliminates the sharp

interfaces where different materials meet and where component failure may be initiated. Here, gradients can generate dissimilar strains resulting in the geometrical morphing of 4D-printed configurations.

4.6.2. Geological Modeling

Graded structures are ubiquitous in nature and many bionic designs involve FGMs.^[229] Functional gradient designs are used in the biosphere and in mimicking ecosystems and lithospheres. For geological models, it is necessary to accurately design these complicated structures, which may involve different sizes of soil pores, water seepage effects, and bearing slip zones. Graded structures in a model can be precisely controlled by FGAM; meanwhile, the mechanical strength and gradient permeability of soil can be reproduced in a 3D printed framework, whereas a gradient in pore size may influence the specific surface area and functionality.^[230] Tang et al.^[231] fabricated a landslide slope model with a graded structure using a slurry deposition method, and used it to accurately simulate natural landslide damage. In conventional geological modeling, the artificial belts in a landslide model are created by thin films and glass beads.^[232] In Tang et al.'s 3D-printed landslide model, water was introduced into the landslide body to build a gradient transition belt between rock and soil (Figure 19a). Using

3D slurry deposition, the study proposed a design of porous slip belts (Figure 19b) that would slide along the stress chain (Figure 19c). Tang et al.^[21] proposed to use a material dispensing AM method to fabricate a transition sliding zone band of certain thickness between the sliding bed and body, with gradients in the stone-soil-wax compositions and porous structures. The study revealed the material-structure-property relationships and analyzed the geomechanics and failure mechanisms of the dual gradient sliding zone band, creating new prospects for landslide research, testing, prediction, and prevention.

5. Future Potential and Prospects

FGAM technology opens new pathways towards the fabrication of multifunctional material systems, enabling more intelligent, rapid and integrated design and fabrication to solve some issues in a wide range of applications. Design of the material-structure-processing-property relationships in FGAM is essential for obtaining the desired multi-functionality. However, until now a lack of established design principles, guidelines and standards for FGAM practices has hindered its evolution, preventing designers or engineers from fully benefiting from this exciting new technology.

This review introduced multi-scale FGAM design principles, including geometrical representation, material distribution,

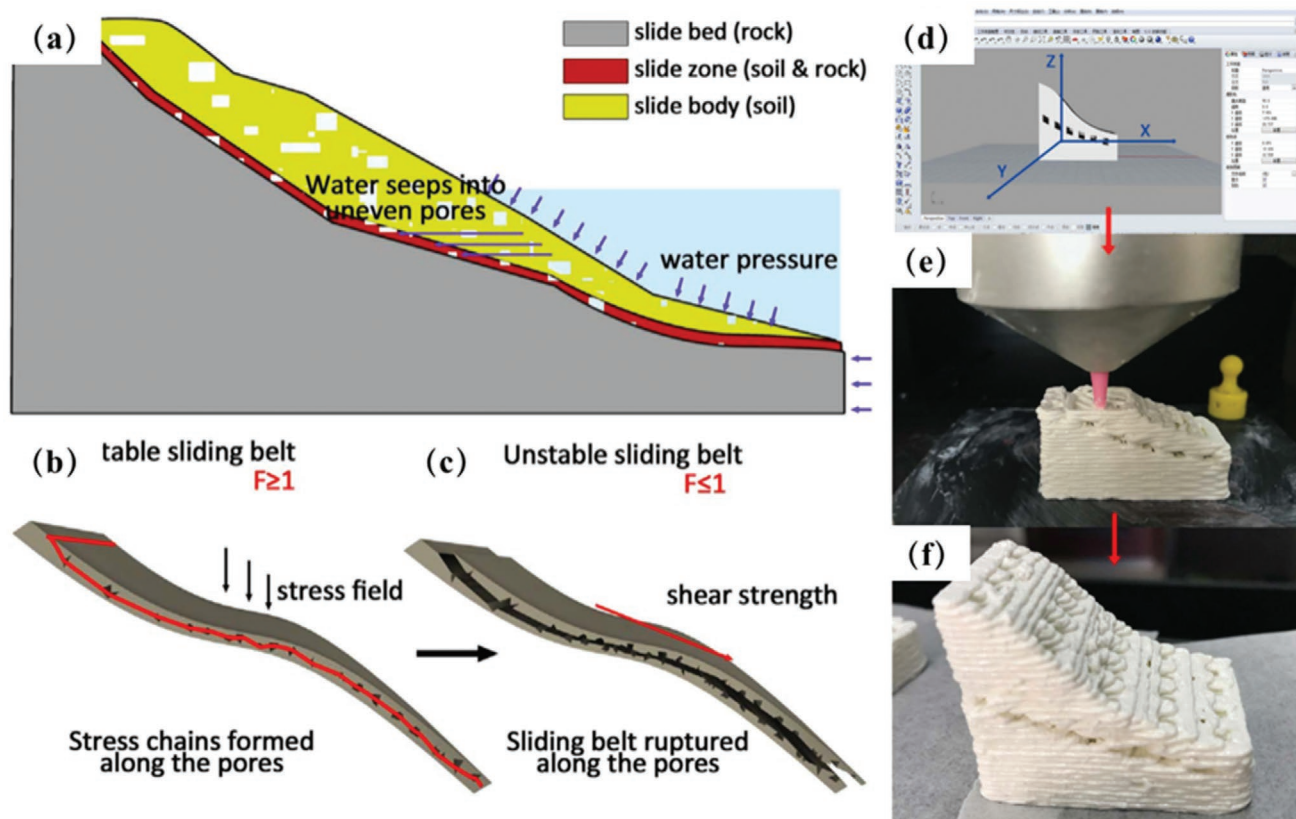


Figure 19. a) Rupture process of a sliding belt. b,c) Porous slip belt and ruptured slip belt, following the Mohr Coulomb failure criterion: when $F \geq 1$, the landslide zone is stable, and when $F \leq 1$, the landslide zone slides. Manufacturing process of small model: d) modeling process; e) 3D printing; f) forming of model. Reproduced with permission.^[231] Copyright 2019, Elsevier.

microstructural designs, and simulation methods. Some of the existing challenges and future trends in the design of FGAM structures are identified and include i) Design for FGAM is multidisciplinary and therefore challenging for designers, engineers, and manufacturers without an appropriate background knowledge in materials science. Guidelines and shared databases integrating materials information (compositions, distributions, compatibility, and gradient dimensions) should be established so that designers, engineers, and manufacturers can avoid undesirable results; ii) Conventional virtual geometrical-based design systems mainly use basic geometrical representations based on a single material. FGAM parts, on the other hand, contain complex internal structures and require a precise distribution of materials at the microstructural level. Therefore, new systematic design systems and simulation software are needed to embed and represent information regarding these materials and to create components more accurately and reliably; iii) Theoretical and numerical models and software capable of simulating physical FGAM processes as well as predicting as-produced geometries, properties, and functional performance of components are needed to provide reliable guidelines for the reconstruction of pre-designed models; iv) In situ and real-time monitoring and characterization are challenging and important in FGAM processes. Suitable analytical techniques through spectroscopic, microscopic and macroscopic means are needed to characterize the nonuniform compositions, structures and properties of FGMs. So far, scientists have creatively proposed various AM technologies for the manufacture of FGMs or FGSSs; however, real industrial applications are still far and few between and still needs significant and comprehensive research efforts in order to solve the large number of issues and challenges involved.

As novel functional materials with complex compositions emerge, newly emerging advanced manufacturing methods must be developed, including novel methods for the creation of FGMs or FGSSs. Micro-nano additive manufacturing (also known as micro-nano scale 3D printing) is a new processing technology for the creation of complex micro-nano structures. FGAM shows potential for the creation of high aspect ratio micro-nano structures, multilateral micro-nano structures, macro/micro-composite structures, and embedded heterostructures.

FGAM also presents opportunities to solve issues in a wide range of applications, including biomedical implants, thermal management, electromagnetic interference shielding (EMI), energy-absorbing systems, optoelectronic devices, and even geological models that simulate natural landslide disasters. The excellent energy-absorbing properties of metamaterials produced via FGAM will promote the evolution of EMI. In addition, gradients can deliver diverse functionalities to multifunctional intelligent materials such as SMM, including controlled morphing of 4D-printed structures. The 4D FGAM technology has the capacity to produce intelligent responsive materials and structures with integrated functions, thereby promoting the development of intelligent manufacturing.

In short, FGAM is creating new avenues to manufacture advanced functional materials with intricate gradients and highly specific properties through precise control of compositions, constituents and structures at multiple length-scales, as

well as the integration of multiple gradients. It is expected that in the not too distant future such advanced multi-materials will be used for the development of novel 3D structures and functional graded devices.

Acknowledgements

The authors gratefully acknowledge financial support from the National Natural Science Foundation of China (No. 51902295, No. 51671091, No. 51675496). The project was also kindly supported by the Fundamental Research Funds for the Central Universities, China University of Geosciences (Wuhan) (No. CUG170677) and Hubei Province Natural Science Foundation grant (No. 2019 CFB264).

Conflict of Interest

The authors declare no conflict of interest.

Keywords

additive manufacturing, functionally graded materials, functionally graded structures, multifunctional properties, multi-scale design

Received: October 31, 2019

Revised: March 8, 2020

Published online: April 29, 2020

- [1] N. Yang, S. Hu, D. Ma, T. Lu, B. Li, *Sci. Rep.* **2015**, 5, 14878.
- [2] G. H. Loh, E. Pei, D. Harrison, M. D. Monzón, *Addit. Manuf.* **2018**, 23, 34.
- [3] U. G. K. Wegst, H. Bai, E. Saiz, A. P. Tomsia, R. O. Ritchie, *Nat. Mater.* **2014**, 14, 23.
- [4] M. Eder, K. Jungnikl, I. Burgert, *Trees* **2009**, 23, 79.
- [5] M. K. Habibi, A. T. Samaei, B. Gheshlaghi, J. Lu, Y. Lu, *Acta Biomater.* **2015**, 16, 178.
- [6] M. Niino, T. Hirai, R. Watanabe, *J. Jpn. Soc. Compos. Mater.* **1987**, 13, 257.
- [7] S. Kumar, K. V. V. S. Murthy Reddy, A. Kumar, G. Rohini Devi, *Aerosp. Sci. Technol.* **2013**, 26, 185.
- [8] S. Hu, A. Gagnoud, Y. Fautrelle, R. Moreau, X. Li, *Sci. Rep.* **2018**, 8, 7945.
- [9] J. Park, K. Park, J. Kim, Y. Jeong, A. Kawasaki, H. Kwon, *Sci. Rep.* **2016**, 6, 23064.
- [10] J. Song, Y. Chew, L. Jiao, X. Yao, S. K. Moon, G. Bi, *Addit. Manuf.* **2018**, 24, 543.
- [11] A. Gupta, M. Talha, *Prog. in Aerosp. Sci.* **2015**, 79, 1.
- [12] F. Xu, X. Zhang, H. Zhang, *Eng. Struct.* **2018**, 171, 309.
- [13] Y. Li, Z. Feng, L. Huang, K. Essa, E. Bilotti, H. Zhang, T. Peijs, L. Hao, *Compos. Part A: Appl. Sci. Manuf.* **2019**, 105483.
- [14] S. A. M. Tofail, E. P. Koumoulos, A. Bandyopadhyay, S. Bose, L. O'Donoghue, C. Charitidis, *Mater. Today* **2018**, 21, 22.
- [15] M. Vaezi, S. Chianrabutra, B. Mellor, S. Yang, *Virtual Phys. Prototyping* **2013**, 8, 19.
- [16] B. Yuan, G. M. Guss, A. C. Wilson, S. P. Hau-Riege, P. J. DePond, S. McMains, M. J. Matthews, B. Giera, *Adv. Mater. Technol.* **2018**, 3, 1870051.
- [17] C. Kenel, P. Schloth, S. Van Petegem, J. L. Fife, D. Grolimund, A. Menzel, H. Van Swygenhoven, C. Leinenbach, *JOM* **2016**, 68, 978.

- [18] P. J. DePond, G. Guss, S. Ly, N. P. Calta, D. Deane, S. Khairallah, M. J. Matthews, *Mater. Des.* **2018**, *154*, 347.
- [19] V. Birman, in *Encyclopedia of Thermal Stresses* (Eds: R. B. Hetnarski), Springer, Dordrecht **2014**, pp. 3104–3112.
- [20] S. Lim, R. A. Buswell, T. T. Le, S. A. Austin, A. G. F. Gibb, T. Thorpe, *Autom. Constr.* **2012**, *21*, 262.
- [21] D. Tang, L. Hao, Y. Li, Z. Li, S. Dadbakhsh, *J. Alloys Compd.* **2020**, *814*, 152275.
- [22] Z. Liu, M. A. Meyers, Z. Zhang, R. O. Ritchie, *Prog. Mater. Sci.* **2017**, *88*, 467.
- [23] C. Bader, D. Kolb, J. C. Weaver, S. Sharma, A. Hosny, J. Costa, N. Oxman, *Sci. Adv.* **2018**, *4*, eaas865.
- [24] <https://www.stratasy.com/software> [accessed 6 March **2020**].
- [25] <https://www.e-xstream.com/industries/additive-manufacturing> [accessed 6 March **2020**].
- [26] A. A. G. Requicha, in *Computer Aided Design Modelling, Systems Engineering, CAD-Systems. Lecture Notes in Computer Science*, Vol 89 (Eds: J. Encarnacao), Springer, Berlin, Heidelberg **1980**, pp. 1–78.
- [27] B. Ripley, T. Kelil, M. K. Cheezum, A. Goncalves, M. F. Di Carli, F. J. Rybicki, M. Steigner, D. Mitsouras, R. Blankstein, *J. Cardiovasc. Comput. Tomogr.* **2016**, *10*, 28.
- [28] P. Yang, D. Du, Z. Zhou, N. Lu, Q. Fu, J. Ma, L. Zhao, A. Chen, *Injury* **2016**, *47*, 2816.
- [29] J. Minnema, M. van Eijnatten, W. Kouw, F. Diblen, A. Mendrick, J. Wolff, *Comput. Biol. Med.* **2018**, *103*, 130.
- [30] M. van Eijnatten, R. van Dijk, J. Dobbe, G. Streekstra, J. Koivisto, J. Wolff, *Med. Eng. Phys.* **2018**, *51*, 6.
- [31] S. Singh, S. Ramakrishna, *Curr. Opin. Biomed. Eng.* **2017**, *2*, 105.
- [32] A. A. Giannopoulos, D. Mitsouras, S. J. Yoo, P. P. Liu, Y. S. Chatzizisis, F. J. Rybicki, *Nat. Rev. Cardiol.* **2016**, *13*, 701.
- [33] K. K. Kumamaru, B. E. Hoppel, R. T. Mather, F. J. Rybicki, *Radiol. Clin. N. Am.* **2010**, *48*, 213.
- [34] O. Sigmund, *Struct. Multidiscipl. Optim.* **2001**, *21*, 120.
- [35] K. Svanberg, *Int. J. Numer. Methods. Eng.* **1987**, *24*, 359.
- [36] M. P. Bendsøe, N. Kikuchi, *Comput. Methods. Appl. Mech. Eng.* **1988**, *71*, 197.
- [37] M. P. Bendsøe, *Struct. Optim.* **1989**, *1*, 193.
- [38] M. P. Bendsøe, in *Encyclopedia of Optimization* (Ed.: C. Floudas), Springer, Boston, MA **2008** pp. 3928–3929.
- [39] S. Osher, J. A. Sethian, *J. Comput. Phys.* **1988**, *79*, 12.
- [40] Fulma, P. Ski, A. Laurain, J. F. Scheid, Soko, J. Owski, *J. Appl. Math. Comput. Sci.* **2007**, *17*, 413.
- [41] J. A. Norato, M. P. Bendsøe, R. B. Haber, D. A. Tortorelli, *Struct. Multidiscipl. Optim.* **2007**, *33*, 375.
- [42] Y. M. Xie, G. P. Steven, *Comput. Struct.* **1993**, *49*, 885.
- [43] G. I. N. Rozvany, *Struct. Multidiscipl. Optim.* **2001**, *21*, 109.
- [44] A. Panesar, M. Abdi, D. Hickman, I. Ashcroft, *Addit. Manuf.* **2018**, *19*, 81.
- [45] D. Li, W. Liao, N. Dai, G. Dong, Y. Tang, Y. M. Xie, *Comput.-Aided Des.* **2018**, *104*, 87.
- [46] Y. Wang, L. Zhang, S. Daynes, H. Zhang, S. Feih, M. Y. Wang, *Mater. Des.* **2018**, *142*, 114.
- [47] T. Liu, S. Guessasma, J. Zhu, W. Zhang, S. Belhabib, *Eur. Polym. J.* **2018**, *108*, 199.
- [48] L. Cheng, J. Bai, A. C. To, *Comput. Methods. Appl. Mech. Eng.* **2019**, *344*, 334.
- [49] M. Jansen, O. Pierard, *Comput. Struct.* **2020**, *231*, 106205.
- [50] W. Roux, G. Yi, I. Gandikota, *Comput. Methods. Appl. Mech. Eng.* **2020**, *361*, 112794.
- [51] D.-m. Xiao, Y.-q. Yang, X.-b. Su, D. Wang, Z.-y. Luo, *Trans. Nonferrous Met. Soc. China* **2012**, *22*, 2554.
- [52] A. Takezawa, Y. Koizumi, M. Kobashi, *Addit. Manuf.* **2017**, *18*, 194.
- [53] T. H. Weisgraber, T. Metz, C. M. Spadaccini, E. B. Duoss, W. Small, J. M. Lenhardt, R. S. Maxwell, T. S. Wilson, *J. Mater. Res.* **2018**, *33*, 1.
- [54] A. O. Aremu, J. P. J. Brennan-Craddock, A. Panesar, I. A. Ashcroft, R. J. M. Hague, R. D. Wildman, C. Tuck, *Addit. Manuf.* **2017**, *13*, 1.
- [55] W. Liu, X. Cheng, *CIRP* **2018**, *78*, 138.
- [56] E. L. Doubrovski, E. Y. Tsai, D. Dikovskiy, J. M. P. Geraedts, H. Herr, N. Oxman, *Comput.-Aided Des.* **2015**, *60*, 3.
- [57] S. Tibbitts, *Archit. Des.* **2014**, *84*, 116.
- [58] G. Sossou, F. Demoly, H. Belkebir, H. J. Qi, S. Gomes, G. Montavon, *Mater. Des.* **2019**, *175*, 107798.
- [59] J. Duro-Royo, N. Oxman, *MRS Proc.* **2015**, *1800*, Mrss15.
- [60] V. Gupta, P. Tandon, *Comput.-Aided Des.* **2015**, *62*, 236.
- [61] W. K. Chiu, S. T. Tan, *Comput.-Aided Des.* **2000**, *32*, 707.
- [62] X. Y. Kou, S. T. Tan, *Comput.-Aided Des.* **2007**, *39*, 284.
- [63] B. Zhang, P. Jaiswal, R. Rai, S. Nelaturi, *J. Comput. Inf. Sci. Eng.* **2018**, *18*, 041002.
- [64] S. Bhashyam, K. H. Shin, D. Dutta, *Rapid Prototyp. J.* **2000**, *6*, 119.
- [65] M. Vaezi, S. Chianrabutra, B. Mellor, S. Yang, *Virtual Phys. Prototyping* **2013**, *8*, 19.
- [66] J. Wang, Z. Pan, Y. Ma, Y. Lu, C. Shen, D. Cuiuri, H. Li, *Mater. Sci. Eng., A* **2018**, *734*, 110.
- [67] L. D. Bobbio, R. A. Otis, J. P. Borgonia, R. P. Dillon, A. A. Shapiro, Z.-K. Liu, A. M. Beese, *Acta. Mater.* **2017**, *127*, 133.
- [68] B. E. Carroll, R. A. Otis, J. P. Borgonia, J.-o. Suh, R. P. Dillon, A. A. Shapiro, D. C. Hofmann, Z.-K. Liu, A. M. Beese, *Acta. Mater.* **2016**, *108*, 46.
- [69] Y. Kok, X. P. Tan, P. Wang, M. L. S. Nai, N. H. Loh, E. Liu, S. B. Tor, *Mater. Des.* **2018**, *139*, 565.
- [70] L. Zhou, H. Pan, H. Hyer, S. Park, Y. Bai, B. McWilliams, K. Cho, Y. Sohn, *Scr. Mater.* **2019**, *158*, 24.
- [71] D. C. Hofmann, S. Roberts, R. Otis, J. Kolodziejska, R. P. Dillon, J.-o. Suh, A. A. Shapiro, Z.-K. Liu, J.-P. Borgonia, *Sci. Rep.* **2014**, *4*.
- [72] T. Wang, Y. Y. Zhu, S. Q. Zhang, H. B. Tang, H. M. Wang, *J. Alloys Compd.* **2015**, *632*, 505.
- [73] W. Xiong, L. Hao, Y. Li, D. Tang, Q. Cui, Z. Feng, C. Yan, *Mater. Des.* **2019**, *170*, 107697.
- [74] J. Lin, D. Guo, Y. Lv, Y. Liu, X. Wu, B. Xu, G. Xu, B. Xu, *Mater. Des.* **2018**, *157*, 200.
- [75] X. Tan, Y. Kok, Y. J. Tan, G. Vastola, Q. X. Pei, G. Zhang, Y.-W. Zhang, S. B. Tor, K. F. Leong, C. K. Chua, *J. Alloys Compd.* **2015**, *646*, 303.
- [76] L. Thijs, K. Kempen, J. P. Kruth, J. V. Humbeeck, *Acta Mater.* **2013**, *61*, 1809.
- [77] T. Ishimoto, K. Hagihara, K. Hisamoto, S. H. Sun, T. Nakano, *Scr. Mater.* **2017**, *132*, 34.
- [78] B. Ferrar, L. Mullen, E. Jones, R. Stamp, C. J. Sutcliffe, *J. Mater. Process. Technol.* **2012**, *212*, 355.
- [79] D. C. Hofmann, J. Kolodziejska, S. Roberts, R. Otis, R. P. Dillon, J.-O. Suh, Z.-K. Liu, J.-P. Borgonia, *J. Mater. Res.* **2014**, *29*, 1899.
- [80] J. S. Zuback, T. A. Palmer, T. DebRoy, *J. Alloys Compd.* **2019**, *770*, 995.
- [81] A. R. Moustafa, A. Durga, G. Lindwall, Z. C. Cordero, *Addit. Manuf.* **2020**, *32*, 101008.
- [82] C. A. Gandin, J. L. Desbiolles, M. Rappaz, Thevoz, *Metall. Mater. Trans. A* **1999**, *30*, 3153.
- [83] A. Zinoviev, O. Zinovieva, V. Ploshikhin, V. Romanova, R. Balokhonov, *Mater. Des.* **2016**, *106*, 321.
- [84] A. Rai, M. Markl, C. Körner, *Comput. Mater. Sci.* **2016**, *124*, 37.
- [85] T. M. Rodgers, J. D. Madison, V. Tikare, M. C. Maguire, *JOM* **2016**, *68*, 1419.
- [86] E. Popova, T. M. Rodgers, X. Gong, A. Cecen, J. D. Madison, S. R. Kalidindi, *Int. Mater. Manuf. Innovation* **2017**, *6*, 54.
- [87] T. Mukherjee, J. S. Zuback, W. Zhang, T. DebRoy, *Comput. Mater. Sci.* **2018**, *143*, 325.
- [88] J. Parthasarathy, B. Starly, S. Raman, *J. Manuf. Process.* **2011**, *13*, 160.

- [89] J. C. Steuben, A. P. Iliopoulos, J. G. Michopoulos, *Comput.-Aided Des.* **2016**, 77, 107.
- [90] H. E. Burton, N. M. Eisenstein, B. M. Lawless, P. Jamshidi, M. A. Segarra, O. Addison, D. E. T. Shepherd, M. M. Attallah, L. M. Grover, S. C. Cox, *Mater. Sci. Eng. C Mater. Biol. Appl.* **2019**, 94, 901.
- [91] E. Salcedo, D. Baek, A. Berndt, J. E. Ryu, *Addit. Manuf.* **2018**, 22, 351.
- [92] L. Ren, Z. Song, H. Liu, Q. Han, C. Zhao, B. Derby, Q. Liu, L. Ren, *Mater. Des.* **2018**, 156, 470.
- [93] D. Kokkinis, F. Bouville, A. R. Studart, *Adv. Mater.* **2018**, 30.
- [94] O. Weeger, N. Boddetti, S. K. Yeung, S. Kaijima, M. L. Dunn, *Addit. Manuf.* **2019**, 25, 39.
- [95] G. Vastola, G. Zhang, Q. X. Pei, Y. W. Zhang, *JOM* **2016**, 68, 1370.
- [96] Y. Lu, Y. Huang, J. Wu, *J. Alloys Compd.* **2018**, 766, 506.
- [97] T. M. Rodgers, J. D. Madison, V. Tikare, *Comput. Mater. Sci.* **2017**, 135, 78.
- [98] J. C. Steuben, A. J. Birnbaum, J. G. Michopoulos, A. P. Iliopoulos, *Addit. Manuf.* **2019**, 25, 437.
- [99] H. L. Wei, J. Mazumder, T. DebRoy, *Sci. Rep.* **2015**, 5, 16446.
- [100] Y. Zhang, D. Kong, S. Liu, *Int. Commun. Heat Mass Transfer.* **2018**, 98, 67.
- [101] M. Naebe, K. Shirvanimoghaddam, *Appl. Mater. Today* **2016**, 5, 223.
- [102] M. Sasaki, T. Hirai, *J. Eur. Ceram. Soc.* **1994**, 14, 257.
- [103] S. Seiffried, M. Winterer, H. Hahn, *Scr. Mater.* **2001**, 44, 2165.
- [104] X. Wang, X. Chu, H. Zhao, S. Lu, F. Fang, J. Li, X. Fang, Z. Wei, X. Wang, P. Du, *Integr. Ferroelectr.* **2014**, 151, 1.
- [105] R. B. Heimann, in *Plasma-spray Coating*, (Eds: R. B. Heimann), John Wiley & Sons, Weinheim, Germany **1996**, pp. 17–25.
- [106] K. A. Khor, Y. W. Gu, *Mater. Sci. Eng., A* **2000**, 277, 64.
- [107] M. Ivošević, R. Knight, S. R. Kalidindi, G. R. Palmese, J. K. Sutter, *J. Therm. Spray Technol.* **2005**, 14, 45.
- [108] A. H. Pakseresht, A. H. Javadi, M. Nejati, K. Shirvanimoghaddam, E. Ghasali, R. Teimouri, *Int. J. Adv. Manuf. Technol.* **2014**, 75, 739.
- [109] A. H. Pakseresht, E. Ghasali, M. Nejati, K. Shirvanimoghaddam, A. H. Javadi, R. Teimouri, *Int. J. Adv. Manuf. Technol.* **2015**, 76, 1031.
- [110] J. Guo, Z. Fang, P. Fan, X. Wang, *Acta Mater.* **2011**, 59, 4719.
- [111] C. Liang, W. Ma, Z. Feng, C. Li, *Carbon* **2003**, 41, 1833.
- [112] A. Zhecheva, W. Sha, S. Malinov, A. Long, *Surf. Coat. Technol.* **2005**, 200, 2192.
- [113] S. G. Fishman, *JOM* **1998**, 40, 8.
- [114] P. X. Fu, X. H. Kang, Y. C. Ma, K. Liu, D. Z. Li, Y. Y. Li, *Intermetallics* **2008**, 16, 130.
- [115] A. G. Arsha, E. Jayakumar, T. P. D. Rajan, V. Antony, B. C. Pai, *Mater. Des.* **2015**, 88, 1201.
- [116] R. Mahmoodian, M. Hassan, M. Hamdi, R. Yahya, R. Rahbari, *Compos. Part B: Eng.* **2014**, 59, 279.
- [117] D. M. Matson, Z. A. Munir, *Mater. Sci. Eng., A* **1992**, 153, 700.
- [118] X. H. Zhang, J. C. Han, S. Y. Du, J. V. Wood, *J. Mater. Sci.* **2000**, 35, 1925.
- [119] I. J. Shon, Z. A. Munir, *J. Am. Ceram. Soc.* **2010**, 81, 3243.
- [120] D. Hotza, P. Greil, *Mater. Sci. Eng., A* **1995**, 202, 206.
- [121] J. G. Yeo, Y. G. Jung, S. C. Choi, *Mater. Lett.* **1998**, 37, 304.
- [122] C. Tallon, G. V. Franks, *J. Ceram. Soc. Jpn.* **2011**, 119, 147.
- [123] S. H. Park, J. H. Kang, Y. G. Jung, U. Paik, *AIP Conf. Proc.* **2008**, 379, 273.
- [124] H. Farnoush, J. A. Mohandesi, H. Çimenoglu, *J. Mech. Behav. Biomed. Mater.* **2015**, 46, 31.
- [125] S. Put, J. Vleugels, G. Anné, O. V. D. Biest, *Colloids Surf., A* **2003**, 222, 223.
- [126] L. Besra, M. Liu, *Prog. Mater. Sci.* **2007**, 52, 1.
- [127] C. Q. Hong, X. H. Zhang, W. J. Li, J. C. Han, S. H. Meng, *Mater. Sci. Eng., A* **2008**, 498, 437.
- [128] J. M. Wilson, Y. C. Shin, *Surf. Coat. Technol.* **2012**, 207, 517.
- [129] J. Ma, G. E. B. Tan, *J. Mater. Process. Technol.* **2001**, 113, 446.
- [130] G. Jin, M. Takeuchi, S. Honda, T. Nishikawa, H. Awaji, *Mater. Chem. Phys.* **2005**, 89, 238.
- [131] A. Standard, *ASTM F2792-10e1* **2012**.
- [132] S. M. Thompson, L. Bian, N. Shamsaei, A. Yadollahi, *Addit. Manuf.* **2015**, 8, 36.
- [133] T. T. Qian, D. Liu, X. J. Tian, C. M. Liu, H. M. Wang, *Trans. Nonferrous Met. Soc. China* **2014**, 24, 2729.
- [134] C. L. Ming, B. K. Leuser, L. Tang, R. G. Landers, G. E. Hilmas, J. L. Watts, *CIRP Ann.* **2012**, 61, 223.
- [135] S. E. Bakarich, R. Gorkin, R. Gately, S. Naficy, M. in het Panhuis, G. M. Spinks, *Addit. Manuf.* **2017**, 14, 24.
- [136] H. Chung, S. Das, *Mater. Sci. Eng., A* **2008**, 487, 251.
- [137] K. Essa, H. Hassanin, M. M. Attallah, N. J. Adkins, A. J. Musker, G. T. Roberts, N. Tenev, M. Smith, *Appl. Catal., A* **2017**, 542, 125.
- [138] T. Niendorf, S. Leuders, A. Riemer, F. Brenne, T. Tröster, H. A. Richard, D. Schwarze, *Adv. Eng. Mater.* **2014**, 16, 857.
- [139] I. Maskery, N. T. Aboulkhair, A. O. Aremu, C. J. Tuck, I. A. Ashcroft, R. D. Wildman, R. J. M. Hague, *Mater. Sci. Eng., A* **2016**, 670, 264.
- [140] S. Y. Choy, C. N. Sun, K. F. Leong, J. Wei, *Mater. Des.* **2017**, 131, 112.
- [141] S. Kumar, *CIRP J. Manuf. Sci. Technol.* **2010**, 3, 85.
- [142] M. P. de Beer, H. L. van der Laan, M. A. Cole, R. J. Whelan, M. A. Burns, T. F. Scott, *Sci. Adv.* **2019**, 5, eaau8723.
- [143] B. E. Kelly, I. Bhattacharya, H. Heidari, M. Shusteff, C. M. Spadaccini, H. K. Taylor, *Science* **2019**, 363, 1075.
- [144] W. Li, S. Karnati, Y. Zhang, F. Liou, *J. Mater. Process. Technol.* **2018**, 254, 294.
- [145] S. Hocine, H. Van Swygenhoven, S. Van Petegem, C. S. T. Chang, T. Maimaitiyili, G. Tinti, D. Ferreira Sanchez, D. Grolimund, N. Casati, *Mater. Today* <https://doi.org/10.1016/j.mattod.2019.10.001>.
- [146] C. Shen, X. Hua, M. Reid, K.-D. Liss, G. Mou, Z. Pan, Y. Huang, H. Li, *J. Alloys Compd.* **2020**, 826, 154097.
- [147] J. L. Bartlett, F. M. Heim, Y. V. Murty, X. Li, *Addit. Manuf.* **2018**, 24, 595.
- [148] S. A. Shevchik, C. Kenel, C. Leinenbach, K. Wasmer, *Addit. Manuf.* **2018**, 21, 598.
- [149] X. Zhang, L. Guo, F. Yang, A. A. Volinsky, M. Hostetter, Z. Guo, *J. Mater. Sci.* **2018**, 54, 2122.
- [150] L. Yang, R. Mertens, M. Ferrucci, C. Yan, Y. Shi, S. Yang, *Mater. Des.* **2019**, 162, 394.
- [151] Q. Wang, S. Zhang, C.-H. Zhang, C.-L. Wu, L. Ren, J.-Q. Wang, J. Chen, *Acta Metall. Sin. (Engl. Lett.)* **2017**, 31, 19.
- [152] L. D. Bobbio, B. Bocklund, R. Otis, J. P. Borgonia, R. P. Dillon, A. A. Shapiro, B. Mcenerney, Z. K. Liu, A. M. Beese, *J. Alloys Compd.* **2018**, 742, 1031.
- [153] R. M. Mahamood, E. T. Akinlabi, *Mater. Des.* **2015**, 84, 402.
- [154] A. J. M. Reichardt, *Design* **2016**, 104, 404.
- [155] L. Wei, S. Karnati, C. Kriewall, F. Liou, J. Newkirk, K. M. B. Taminger, W. J. Seufzer, *Addit. Manuf.* **2017**, 14, 95.
- [156] Y. Liu, C. Liang, W. Liu, Y. Ma, C. Liu, C. Zhang, *J. Alloys Compd.* **2018**, 763, 376.
- [157] D. D. Lima, S. A. Mantri, C. V. Mikler, R. Contieri, C. J. Yannetta, K. N. Campo, E. S. Lopes, M. J. Styles, T. Borkar, R. Caram, R. Banerjee, *Mater. Des.* **2017**, 130, 8.
- [158] M. Ni, C. Chen, X. Wang, P. Wang, R. Li, X. Zhang, K. Zhou, *Mater. Sci. Eng., A* **2017**, 701, 344.
- [159] Y. Li, H. Jahr, P. Pavanram, F. S. L. Bobbert, U. Paggi, X. Y. Zhang, B. Pouran, M. A. Leeftang, H. Weinans, J. Zhou, A. A. Zadpoor, *Acta Biomater.* **2019**, 96, 646.
- [160] R. Luquan, S. Zhengyi, L. Huili, H. Qinghe, Z. Che, D. Brian, L. Qingping, R. J. M. Lei, *Mater. Des.* **2018**, 156, 470.
- [161] S. Yu, J. Sun, J. Bai, *Mater. Des.* **2019**, 182, 108021.

- [162] M. Mahbod, M. Asgari, *Int. J. Mech. Sci.* **2019**, *155*, 248.
- [163] Y. Zhang, J. Han, X. Zhang, X. He, Z. Li, S. Du, *Mater. Sci. Eng., A* **2001**, *299*, 218.
- [164] J. M. Shi, L. X. Zhang, Q. Chang, Z. Sun, J. C. Feng, *Ceram. Int.* **2018**, *44*, 11060.
- [165] H. Seitz, W. Rieder, S. Irsen, B. Leukers, C. Tille, *J. Biomed. Mater. Res., Part B* **2005**, *74*, 782.
- [166] P. Y. Chen, A. Y. M. Lin, Y. S. Lin, Y. Seki, A. G. Stokes, J. Peyras, E. A. Olefsky, M. A. Meyers, J. McKittrick, *J. Mech. Behav. Biomed. Mater.* **2008**, *1*, 208.
- [167] J. Enax, O. Prymak, D. Raabe, M. Epple, *J. Struct. Biol.* **2012**, *178*, 290.
- [168] B. Bar-On, F. G. Barth, P. Fratzl, Y. Politi, *Nat. Commun.* **2014**, *5*, 3894.
- [169] Y. Politi, M. Prieswasser, E. Pippel, P. Zaslansky, J. Hartmann, S. Siegel, C. Li, F. G. Barth, P. Fratzl, *Adv. Funct. Mater.* **2012**, *22*, 2519.
- [170] W. Yang, I. H. Chen, B. Gludovatz, E. A. Zimmermann, R. O. Ritchie, M. A. Meyers, *Adv. Mater.* **2013**, *25*, 31.
- [171] B. J. F. Bruet, J. Song, M. C. Boyce, C. Ortiz, *Nat. Mater.* **2008**, *7*, 748.
- [172] A. R. Studart, *Angew. Chem., Int. Ed.* **2015**, *54*, 3400.
- [173] P. Fratzl, F. G. Barth, *Nature* **2009**, *462*, 442.
- [174] M. A. Meyers, J. McKittrick, P.-Y. Chen, *Science* **2013**, *339*, 773.
- [175] D. Jiao, Z. Q. Liu, R. T. Qu, Z. F. Zhang, *Mater. Sci. Eng., C* **2016**, *59*, 828.
- [176] F. Barthelat, Z. Yin, M. J. Buehler, *Nat. Rev. Mater.* **2016**, *1*, 16007.
- [177] A. R. Studart, R. Libanori, R. M. Erb, in *Bio- and Bioinspired Nanomaterials*, (Eds: D. Ruiz-Molina, F. Novio, C. Roscini), Wiley-VCH, Weinheim, Germany **2014**, Ch. 13.
- [178] L. K. Grunenfelder, N. Suksangpanya, C. Salinas, G. Milliron, N. Yaraghi, S. Herrera, K. Evans-Lutterodt, S. R. Nutt, P. Zavattieri, D. Kisailus, *Acta Biomater.* **2014**, *10*, 3997.
- [179] T. Hoc, L. Henry, M. Verdier, D. Aubry, L. Sedel, A. Meunier, *Bone* **2006**, *38*, 466.
- [180] J. J. Martin, B. E. Fiore, R. M. Erb, *Nat. Commun.* **2015**, *6*, 8641.
- [181] S. E. Bakarich, R. Gorkin, M. in het Panhuis, G. M. Spinks, *ACS Appl. Mater. Interfaces* **2014**, *6*, 15998.
- [182] C. Han, Y. Li, Q. Wang, S. Wen, Q. Wei, C. Yan, L. Hao, J. Liu, Y. Shi, *J. Mech. Behav. Biomed. Mater.* **2018**, *80*, 119.
- [183] M. Monzón, C. Liu, S. Ajami, M. Oliveira, R. Donate, V. Ribeiro, R. L. Reis, *Bio-Des. Manuf.* **2018**, *1*, 69.
- [184] Z. Feng, Y. Li, C. Xin, D. Tang, W. Xiong, H. Zhang, *C* **2019**, *5*, 25.
- [185] M. Costantini, J. Jaroszewicz, L. Kozon, K. Szlazak, W. Swieszkowski, P. Garstecki, C. Stubenrauch, A. Barbetta, J. Guzowski, *Angew. Chem., Int. Ed.* **2019**, *58*, 7620.
- [186] C. Han, Y. Li, Q. Wang, D. Cai, Q. Wei, L. Yang, S. Wen, J. Liu, Y. Shi, *Mater. Des.* **2018**, *141*, 256.
- [187] T. Kawai, Y. Shanjani, S. Fazeli, A. W. Behn, Y. Okuzu, S. B. Goodman, Y. P. Yang, *J. Orthop. Res.* **2018**, *36*, 1002.
- [188] L. Mogas-Soldevila, J. Duro-Royo, N. Oxman, *3D Print. Addit. Manuf.* **2014**, *1*, 141.
- [189] M. Maruyama, A. Nabeshima, C. C. Pan, A. W. Behn, T. Thio, T. Lin, J. Pajarinen, T. Kawai, M. Takagi, S. B. Goodman, Y. P. Yang, *Biomaterials* **2018**, *187*, 39.
- [190] T. J. Klein, S. C. Rizzi, J. C. Reichert, G. Nicole, M. Jos, S. Wouter, R. W. Crawford, D. W. Huttmacher, *Macromol. Biosci.* **2010**, *9*, 1049.
- [191] W. Sun, B. Starly, A. Darling, C Gomez, *Biotechnol. Appl. Biochem.* **2010**, *39*, 49.
- [192] S. G. Mosanenzadeh, H. E. Naguib, C. B. Park, N. Atalla, *J. Mater. Sci.* **2015**, *50*, 1248.
- [193] B. Chen, X. Huang, D. Gou, J. Zeng, G. Chen, M. Pang, Y. Hu, Z. Zhao, Y. Zhang, Z. Zhou, H. Wu, H. Cheng, Z. Zhang, C. Xu, Y. Li, L. Chen, A. Wang, *Biomed. Opt. Express* **2018**, *9*, 1992.
- [194] V. Weißmann, R. Bader, H. Hansmann, N. Laufer, *Mater. Des.* **2016**, *95*, 188.
- [195] K. B. Hazlehurst, C. J. Wang, M. Stanford, *Mater. Des.* **2014**, *60*, 177.
- [196] K. B. Hazlehurst, C. J. Wang, M. Stanford, *Med. Eng. Phys.* **2014**, *36*, 458.
- [197] L. Wang, J. Kang, C. Sun, D. Li, Y. Cao, Z. Jin, *Mater. Des.* **2017**, *133*, 62.
- [198] X.-Y. Zhang, G. Fang, L.-L. Xing, W. Liu, J. Zhou, *Mater. Des.* **2018**, *157*, 523.
- [199] M. Fousova, D. Vojtech, J. Kubasek, E. Jablonska, J. Fojt, *J. Mech. Behav. Biomed. Mater.* **2017**, *69*, 368.
- [200] X. Y. Zhang, G. Fang, S. Leeflang, A. A. Zadpoor, J. Zhou, *Acta Biomater.* **2019**, *84*, 437.
- [201] Y. C. Wu, C. N. Kuo, M. Y. Shie, Y. L. Su, L. J. Wei, S. Y. Chen, J. C. Huang, *Mater. Des.* **2018**, *158*, 256.
- [202] B. Onuik, B. Heer, A. Bandyopadhyay, *Addit. Manuf.* **2018**, *21*, 133.
- [203] K. J. Lin, K. M. Hu, D. D. Gu, *Opt. Laser Technol.* **2019**, *115*, 9.
- [204] N. W. Bartlett, M. T. Tolley, J. T. B. Overvelde, J. C. Weaver, B. Mosadegh, K. Bertoldi, G. M. Whitesides, R. J. Wood, *Science* **2015**, *349*, 161.
- [205] J. Feng, Y. Zhang, P. Wang, H. Fan, *Compos. Part B: Eng.* **2016**, *99*, 465.
- [206] L. X. Yin, J. Doyhamboure-Fouquet, X. Y. Tian, D. C. Li, *Compos. Part B: Eng.* **2018**, *132*, 178.
- [207] D. S. J. Al-Saedi, S. H. Masood, M. Faizan-Ur-Rab, A. Alomarah, P. Ponnusamy, *Mater. Des.* **2018**, *144*, 32.
- [208] G. Singh, P. M. Pandey, *Mater. Sci. Eng., A* **2019**, *761*, 138035.
- [209] L. X. Yin, X. Y. Tian, Z. T. Shang, D. C. Li, *Mater. Lett.* **2019**, *239*, 132.
- [210] D. A. Roper, B. L. Good, M. Raymond, Y. Shridhar, S. Jared, G. Austin, P. Peter, M. S. Mirotznik, *Smart Mater. Struct.* **2014**, *23*, 045029.
- [211] A. Good, D. Roper, M. Mirotznik, in *2015 IEEE International Symposium on Antennas and Propagation & USNC/URSI National Radio Science Meeting*, Vancouver, BC **2015**, pp. 1318–1319.
- [212] A. J. Good, D. Roper, B. Good, S. Yarlagadda, M. S. Mirotznik, *Smart Mater. Struct.* **2017**, *26*, 095036.
- [213] Z. Larimore, S. Jensen, P. Parsons, B. Good, K. Smith, M. Mirotznik, *Addit. Manuf.* **2017**, *15*, 48.
- [214] H.-R. Wang, M. J. Cima, B. D. Kernan, E. M. Sachs, *J. Non-Cryst. Solids* **2004**, *349*, 360.
- [215] B. L. Good, D. A. Roper, in *2016 IEEE International Symposium on Antennas and Propagation (APSURSI)*, Fajardo **2016**, pp. 2157–2158.
- [216] A. P. Haring, A. U. Khan, G. Liu, B. N. Johnson, *Adv. Opt. Mater.* **2017**, *5*, 1700367.
- [217] W. Li, X. You, H. Mu, J. Deng, G. Zhang, in *2015 IEEE PES Asia-Pacific Power and Energy Engineering Conference (APPEEC)*, Brisbane, QLD **2015**, pp. 1–4.
- [218] Z. Liu, W. D. Li, Y. B. Wang, G. Q. Su, G. J. Zhang, Y. Cao, D. C. Li, in *2016 IEEE International Conference on High Voltage Engineering and Application (ICHVE)*, Chengdu **2016**, pp. 1–4.
- [219] B. Heer, A. Bandyopadhyay, *Mater. Lett.* **2018**, *216*, 16.
- [220] V. Chaudhary, N. M. Sai Kiran Kumar Yadav, S. A. Mantri, S. Dasari, A. Jagetia, R. V. Ramanujan, R. Banerjee, *J. Alloys Compd.* **2020**, *823*, 153817.
- [221] C. Tan, S. Li, K. Essa, P. Jamshidi, K. Zhou, W. Ma, M. M. Attallah, *Int. J. Mach. Tool. Manuf.* **2019**, *141*, 19.
- [222] S. Li, H. Hassanin, M. M. Attallah, N. J. E. Adkins, K. Essa, *Acta Mater.* **2016**, *105*, 75.
- [223] E. J. Pei, *Assem. Autom.* **2014**, *34*, 123.
- [224] E. J. Pei, G. H. Loh, D. Harrison, H. D. Almeida, M. D. M. Verona, R. Paz, *Assem. Autom.* **2017**, *37*, 147.

- [225] S. D. Miao, W. Zhu, N. J. Castro, J. S. Leng, L. G. Zhang, *Tissue Eng., Part C* **2016**, 22, 952.
- [226] K. Yu, A. Ritchie, Y. Mao, M. L. Dunn, H. J. Qi, *Procedia IUTAM* **2015**, 12, 193.
- [227] M. Bodaghi, A. R. Damanpack, W. H. Liao, *Mater. Des.* **2017**, 135, 26.
- [228] U. Scheithauer, S. Weingarten, R. Johne, E. Schwarzer, J. Abel, H. J. Richter, T. Moritz, A. Michaelis, *Materials* **2017**, 10, 1368.
- [229] J. Duro-Royo, K. Zolotovskiy, L. Mogas-Soldevila, S. Varshney, N. Oxman, M. C. Boyce, C. Ortiz, *Comput.-Aided Des.* **2015**, 60, 14.
- [230] E. C. Hammel, O. L. R. Ighodaro, O. I. Okoli, *Ceram. Int.* **2014**, 40, 15351.
- [231] D. N. Tang, L. Hao, Y. Li, W. Xiong, T. Sun, X. K. Yan, *Compos. Part A: Appl. Sci. Manuf.* **2018**, 108, 99.
- [232] G. Shanmugam, *J. Palaeogeog. English* **2015**, 4, 109.